Population Morphology Implies a Common Developmental Blueprint for *Drosophila* Motion Detectors

Nikolas Drummond[1], Arthur Zhao[2], Alexander Borst[1]*

1 Department of Circuits - Computation - Models, Max Planck Institute for Biological Intelligence, Munich, Germany **2** Reiser Lab, HHMI Janelia Research Campus, Virginia, USA

* alexander.borst@bi.mpg.de

Abstract

Quantitative analysis of neuron morphology is essential in order to develop our understanding of circuit organisation and development. The recent acquisition of whole-brain electron microscopy-based (EM) reconstructions of the *Drosophila melanogaster* nervous system now provide the resolution needed to examine morphology at scale. Utilising these data, together with new computational tools, we extract and analyse the dendrites of all T4 and T5 neurons within one hemisphere ($n \sim 6000$).

T4 and T5 neurons are the first uniquely direction-selective neurons in the visual pathway, and are classified into four subtypes (a,b,c, and d). Each subtype encodes one of four cardinal motion directions (up, down, forwards, backwards). The dendrites of these neurons form in two distinct neuropils, the Medulla (T4) and the Lobula (T5), and are asymmetrically oriented in a direction inverse to the direction of motion which they encode. However, their densely overlapping and compact arbours has made rigorous morphological quantification challenging. The presence of differences beyond their characteristic orientation, both between T4 and T5, as well as within subtypes, has remained poorly understood.

Our analysis reveals a high degree of structural similarity across both types and subtypes. Particularly, measures of geometry and graph topology show only minor variation, with no consistent separation between T4 and T5, or their subtypes.

These results indicate that, despite forming in different neuropils, and serving distinct motion directions, T4 and T5 dendrites follow closely aligned morphological patterns. This suggests that their arborization may be governed by shared developmental constraints and mechanisms.

Introduction

The importance of neuron morphology been recognised within neuroscience for over a century [1–3]. The specific morphology of a neuron dictates its network connectivity [4]. Further, the quantification of neuron morphology can shed light on neuron development, as well as the relationship between structure and function [2, 5].

With the release of a fully reconstructed connectome of an adult female drosophila

brain (FLYWIRE) [6–8], alongside a full inventory of the optic lobe [9], detailed synapse annotations [10, 11], and neurotransmitter type classification [12] the wealth of morphological data within *Drosophila* is unparalleled . Further, with the release of additional publicly available datasets [13, 14], the volume of morphological data in *Drosophila* is unparalleled. These data open exciting avenues in many neuroscientific research directions, from theoretical models [15], to comparative analysis [16, 17], and understanding development [18, 19].

We choose here to focus specifically on the dendrites of T4 and T5 neurons within the drosophila visual system for two key reasons. First, these neurons are amongst the best understood in circuit neuroscience [20, 21]. Second, the large n of these neurons (~ 6000 per optic lobe) offers the opportunity to statistically, and rigorously, compare neuron morphology within a single example dataset. Although single T4 and T5 dendrites can be isolated using sparse labelling methods, their non-tiling, densely overlapping nature, and small size, makes detailed morphological characterization of multiple examples within a single brain using light-level microscopy especially challenging. As such, they are an exceptional candidate for rigorous morphological characterisation utilising connectomics data. By doing so, we shed light on their morphological similarities and differences.

These neurons within *Drosophila melanogaster* are the first uniquely motion direction selective neurons within the *Drosophila* visual system. They process information across three retinotopically arranged neuropils, the Medulla, Lobula and Lobula Plate (Fig. 1,a). T4 neurons respond preferentially to moving light increments (ON-pathway), receiving their inputs in the Medulla and outputting in the Lobula Plate. T5 neurons respond to moving light decrements (OFF-pathway), receiving inputs within the Lobula and again outputting within the Lobula Plate. T4 dendrites innervate Medulla layer 10, where as T5 dendrites innervate Lobula layer 1. Both T4 and T5 cells form four subtypes (a,b,c,d), which encode one of four cardinal directions (up/down, vertical, c and d subtypes; forwards/backwards, horizontal, a and b subtypes) [22]. This directional orientation is dominant within the central region of the eye, and orients in a manner determined by the structure of the compound eye [23]. Additionally, evidence in favour of further functional subtype division along the horizontal axis is given in [24].

The retinotopic mapping of each neuropil is represented through their columnar

structure (Fig. 1,d, insert), and each T4/T5 dendrite spans across approximately seven adjacent columns [25, 26]. Strikingly, each dendrite subtype has an asymmetric orientation inverse to its preferred functional direction (Fig. 1,c). Each T4/T5 dendrite forms synapses with the same set of neuropil specific input partners, in a distinct spatial order, clearly distinguishing the ON and OFF pathways [25].

During development, both T4 and T5 neurons form from the same neuroblasts through a series of binary switches [27] coordinated through a combinatorial code of temporal transcription factors determining subtypes [28]. A single neuroblast will form into a four neurons along the horizontal, or vertical, axis. Specifically, a single neuroblast will form into either a set of T4 a and b and T5 a and b neurons, or T4 c and d and T5 c and d. The final type division during development separates T4 and T5 neurons of the same subtype, for example, T4a and T5a.

Previous work from EM-reconstructions has highlighted the compartmentalized organization of synapses onto T4 and T5 dendrites [25, 29], as well as the relationship between dendritic orientation and preferred direction of motion, linking the observed variability in orientation to the anatomy of the compound eye [23].

Although the genetic origin of the differing subtypes is understood, a fundamental question remains open regarding the morphological similarities and differences between these neurons, and how this may relate to their development. Importantly, the mechanism of their characteristic morphological asymmetry is not yet understood. On the one hand, the differing visual pathways, and tight control of orientation specific input organization required for motion detection may indicate a highly controlled and nuanced process differing between subtypes. On the other hand however, given the similar computation and biophysics, as well as developmental origin, it would seem redundant for multiple algorithms to be employed.

We separate our analysis of T4 and T5 dendrite morphology into three components. First, we examine the spatial embedding and occupied space of these dendrites within their densely overlapping environment. Second, we consider the orientation and geometry of individual dendrites, focusing on the angular properties of bifurcations within the dendrite arborisation. Finally, we examine the topological and graphical structure of T4 and T5 dendrites.

We find a number of interesting differences in terms of the spatial embedding of T4

and T5 dendrites, particularly in relations to their extent of growth along the dorsal-ventral and anterior-posterior axis, and the spatial organisation of dendritic size across their respective neuropil layers. However, the internal geometry and topology is highly conserved across all T4, T5, and their subtypes. These results are in favour of a shared developmental algorithm across both T4 and T5. Additionally, given the observed stereotypy, it is unclear how differences these dendrites characteristic asymmetry could emerge as a direct result of the dendritic growth process alone and is not the result of fundamental morphological differences between these dendrites

Results

Note on Statistical Analysis and Outcomes.

We analysed group differences using ordinary least squares regression models. Main effects of type, subtype, and their interaction were evaluated with analysis of variance (ANOVA). When continuous covariates were included, we used analysis of covariance (ANCOVA) to account for their contribution.

As the sample size in these datasets is large, even extremely small effects can produce very small p-values, which limits the interpretability of significance testing alone [30]. As such we focus on reporting effect sizes in order to emphasise the magnitude of differences over statistical significance alone [31, 32].

For ANOVA and ANCOVA models, we report partial eta squared, η_p^2, which quantifies the proportion of variance uniquely attributed to each factor given the model structure [32] (See Materials and Methods, Statistical Analysis). Guidelines from [33] are used for interpretation: "small" effect size as ≥ 0.02, a "medium" effect size as ≥ 0.13, and a "large" effect size as ≥ 0.26. For continuous covariates we report standardized beta coefficients with equivalent effect size cut-off values ("small": ≥ 0.14, "medium": ≥ 0.36,"large": ≥ 0.51). For post-hoc pairwise comparisons, we report Cohen′s$_d$ ("small": $\geq \pm 0.2$, "medium": $\geq \pm 0.5$,"large": $\geq \pm 0.8$) [33]. As Cohen′s$_d$ is signed, it provides the direction of difference between groups.

In order to quantify uncertainty around effect sizes we additionally compute non-parametric bootstrap confidence intervals (1000 bootstrap replicates). An effect is

considered meaningfully large when both the point estimate and it's entire confidence interval exceed the threshold for a small effect.

T4 and T5 Dendrite Annotation and Pre-processing.

Given the current wealth of morphological data available through the emergence of novel connectomics datasets, tools for handling these data are in their infancy and of pressing importance to the community. Previously, separation of neuron morphologies into biologically relevant sub-trees, such as the axon and dendrite, has been done manually [34] or derived from synapse data as in [35, 36]. Within this dataset of ~ 6000 neurons, manual annotation of each dendrite is not practical. Methods based on the input-to-output ratios of synapses [35, 36] assume clearly defined information flow between compartments, which does not always hold [34], and require additional synapse annotations. We instead implement a novel, semi-automated method to annotate the dendritic compartment of T4 and T5 neurons based on tree structure alone.

Neuron surface meshes available through flywire [7–9, 76] are first skeletonized in order to obtain directed tree-graph representations of each neuron (See Materials and Methods, T4 and T5 Neuron Morphologies; Neuron as Tree Graphs). The correct rooting of each neuron at the soma is then manually verified and corrected if needed. Given a directed tree-graph we define a sub-tree as all nodes and edges downstream of a specified node. Given a correctly rooted neuron skeleton we find the branch node which minimises the total cable length within the sub-tree, and maximises the number of terminal, or leaf, nodes (See Materials and Methods, Dendrite Extraction and Data Pre-processing, Fig. 1,b). A second manual verification of all neurons is then completed in order to ensure that the annotated sub-tree defined by the identified node isolates the complete dendrite. During this second manual review step, the reviewer can additionally fix individual errors in the case where the dendrite sub-tree is clearly defined by a single node. Both manual review steps are completed using a custom built GUI to visualise neurons and manually select nodes. This annotation and review can be completed for ~ 6000 neurons in a short time by a single expert reviewer. Using this pipeline we isolate $\sim 95\%$ of available dendrites for all T4 and T5 neurons within the right optic lobe ($n = 5828$). Supplementary table 1 provides counts and proportions of retained

dendrites for analysis in comparison to all available T4 and T5 neurons by subtype.

As T4 and T5 dendrites exist in two separate neuropils (Fig. 1,a) we also align both sets of dendrites to a common reference space (Fig. 1,d, Materials and Method, Alignment and Scaling). In brief, taking advantage of the fact that both Medulla layer 10 and Lobula layer 1 are well approximated by a section on the surface of a sphere (Fig. 1,d), we first centre the entire T4 and T5 dendrite populations to separate fitted spheres, before rotating and translating each population so that their principle axis align with the polar and equatorial axis of each sphere. Finally, using the column annotation available through flywire (Fig. 1, d insert) we manually orient each population to ensure the correct Dorsal / Ventral / Anterior / Posterior global alignment, without modifying the alignment of the principle axis. This ensure that all T4 and T5 dendrites are aligned to the same Dorsal-Ventral and Anterior-Posterior axis.

Dendrite Spatial Embedding

We first turn to understand the spatial structure and embedding of T4 and T5 dendrites in order to understand differences in the manner by which these dendrites occupy their densely overlapping environment. Here we focus on the shape and volume of the spanned region of T4 and T5 dendrites, the manner by which these dendrites innervate across the depth axis of their respective neuropil layers, and the spatial relationships between the first branching point of different dendrites.

Dendrite Shape

T4 and T5 dendrites are often characterised by their asymmetrical orientation [22], whereby the direction of dendrite outgrowth is inverse to the direction of functionally encoded motion (Fig. 1,c). In order to visualise the occupied space of dendrites by subtypes we align individual dendrites to their internal principle axis, ensuring that the major axis aligns with the y-axis, and scale by the population standard deviation along the y-axis within type (See Materials and Methods, Alignment and Scaling). By centring individual dendrites on the first branch point, we can overlay all dendrites within subtypes (Fig. 2,a). This shows us a clear elliptical spatial occupancy shared across all dendrite subtypes.

Given these dendrites characteristic asymmetry, it is unclear from this alone if the internal principle axis, and the extension of these dendrites in space, is shared along either the dorsal-ventral (DV) or anterior-posterior (AP) axis across all subtypes, or differs between horizontally oriented (a,b) and vertically oriented (c,d) subtypes. In order to investigate this we measure the angle between each dendrites internal principle axis and the global DV axis (Fig. 2,b). We find that the internal principle axis of all types and subtypes is aligned well with the global DV axis (Fig. 2,b). There is no meaningfully large difference between Types ($\eta_p^2 \leq 0.02$). We find a small main effect of Subtypes ($\eta_p^2 = 0.03, \mathrm{CI} : [0.025, 0.039]$). *post-hoc* pairwise comparisons show some variability between subtypes, although all observed effect sizes are small ($0.02 \geq \eta_p^2 \leq 0.13$). Specifically, we find a meaningful but small difference between a→b subtypes ($\eta_p^2 = 0.03, \mathrm{CI} : [0.021, 0.043]$); b→c subtypes ($\eta_p^2 = 0.05, \mathrm{CI} : [0.039, 0.064]$); b→d subtypes ($\eta_p^2 = 0.024, \mathrm{CI} : [0.021, 0.029]$); and c→d subtypes ($\eta_p^2 = 0.06, \mathrm{CI} : [0.054, 0.088]$). To give an idea of the magnitude of the difference, we note that the largest observed absolute difference in mean angles within a subtypes is between b and c subtypes, and is only 17.78°, indicating both subtypes are still aligned around the DV axis, only with some small subtype specific deviation. The interaction term investigating if the pattern is differs between subtypes within types is not meaningful ($\eta_p^2 \leq 0.02$). This indicates that the primary manner of elongation for all T4 and T5 dendrites, as well as subtypes, is along the DV axis.

In order to understand if these dendrites differ in their spread along the DV, AP and depth axis we examine the variance explained along each principle component (PC, Fig. 2,d). Our analysis is conducted within each PC separately. As we have shown that PC1 is aligned well with the DV axis, it follows that PC2 is aligned well with the AP axis, and PC3 aligns well with the depth of each dendrites respective neuropil layer.

Within PC1 we find no meaningful large difference between types $\eta_p^2 \leq 0.02$. Between subtypes we find a medium strength effect ($\eta_p^2 = 0.16, \mathrm{CI} : [0.14, 0.18]$). We find a small effect size when comparing c vs d subtypes Cohen$'\mathrm{s}_d = -0.37, \mathrm{CI} : [-0.32, -0.46]$). Comparisons between a and c subtypes have a medium effect size (Cohen$'\mathrm{s}_d = -0.73, \mathrm{CI} : [-0.63, -0.78]$). comparisons between a and d, b and c, and b and d subtypes all have a large effect size (Cohen$'\mathrm{s}_d \geq -0.8$). The interaction term is not meaningfully large ($\eta_p^2 \leq 0.02$). Looking at the mean differences

between subtypes, there is a clear structuring in this result. The variance explained along the first axis, which translates to the DV axis, is ordered in a subtype specific manner following $b > a > c > d$.

Within PC2 we again find no meaningfully large difference between types ($\eta_p^2 \leq 0.02$), and again a medium effect size between subtypes ($\eta_p^2 = 0.18, \mathrm{CI} : [0.16, 0.20]$). Here, comparisons between the c and d subtypes ($\mathrm{Cohen's}_d = 0.38, \mathrm{CI} : [0.27, 0.42]$) show a small effect size. Between the a and c subtypes ($\mathrm{Cohen's}_d = -0.68, \mathrm{CI} : [0.61, 0.76]$) we find a medium effect size. Comparisons between a and d, b and c, and b and d all show a large effect size ($\mathrm{Cohen's}_d \geq 0.8$). Again, comparing the mean difference between subtypes we find a clear ordering, whereby $d > c > a > b$, which is inverse to that found in PC1. the interaction term is again not meaningfully large ($\eta_p^2 \leq 0.02$).

Within PC3 we find a slightly different result. Here, we observe a small effect of type ($\eta_p^2 = 0.045, \mathrm{CI} : [0.036, 0.055]$). *post-hoc* comparisons show that T4 ¡ T5 with a medium effect size ($\mathrm{Cohen's}_d = -0.68, \mathrm{CI} : [-0.64, -0.74]$). This difference may be a result of the two different neuropils T4 and T5 dendrites innervate. In comparison $\eta_p^2 \leq 0.02$ for both subtype and interaction effects.

Given the orderings observed in PC1 and PC2, we fit an ANCOVA model for PC2 with PC1 as a covariate (Fig. 2,e). With PC1 included as a covariate for PC2, we find a small main effect of type ($\eta_p^2 = 0.031, \mathrm{CI} : [0.022, 0.040]$) as well as strong main effect of PC1 on PC2 $\beta_p = -1.058, \mathrm{CI} : [-1.033, -1.083]$, showing a strong negative relationship between PC1 and PC2. Additionally, the interaction term between type and PC1 also shows a strong effect ($\beta_p = -1.058, \mathrm{CI} : [-1.033, -1.083]$). The interaction term tells us their are differing slopes between T4 and T5 ($\Delta\beta_p = -0.188, \mathrm{CI} : [-0.169, -0.207]$), where this relationship is stronger in T4 than in T5 (Fig. 2,e). We see no difference between subtypes, or other interaction terms however ($\eta_p^2 \leq 0.02; \beta_p \leq 0.14$).

Together, these results tell us that all T4 and T5 dendrites elongate primarily along the DV axis in both the Medulla and Lobula. However the extent of this elongation is mediated by subtype, although in the same manner between T4 and T5. Interestingly, the observed negative correlation between the dendritic spread along the DV and AP axis indicates that the greater the extent of outgrowth along the DV axis, the lesser the extend along the AP axis in a proportional manner.

Dendrite Volume

Having established the shape of T4 and T5 dendrites we next turn to investigate the spanned volume of each dendrite. Previous work has shown that T4 and T5 dendrites span across approximately seven visual columns in both the Medulla and Lobula [25, 26]. This is done by fitting a convex hull to the each individual dendrite morphology (Fig. 2,f). Here we find a small main effect of type ($\eta_p^2 = 0.046, \mathrm{CI} : [0.037, 0.057]$). *Post-hoc* comparisons indicate a medium sized effect indicating that mean absolute T4 volume is greater than T5 ($\mathrm{Cohen's}_d = -0.611, \mathrm{CI} : [-0.564, -0.657]$, Fig. 2,f). The effect size for both subtype and type:subtype interaction is not meaningfully large ($\eta_p^2 \leq 0.02$).

However, the Medulla is notably larger than the Lobula. In order to account for this difference we scale dendrite convex hull volumes by the volume of a surface mesh for Medulla layer 10 for T4 and Lobula layer 1 for T5 (See Materials and Methods, Surface Fitting, Volume, and Depth Measurement). Once doing so, all type, subtype and interaction effect are no longer meaningfully large $\eta_p^2 \leq 0.02$ (Fig. 2,g). This indicates that the mean proportional volume is the same across all types and subtype, as would be expected from each dendrite spanning seven equivalent columns in space.

We note however that the distribution of T4 volumes is notably more heavy tailed than that of T5 (Fig. 2,f and g; Fig. S1). When we look at the volume of T4 and T5 dendrites plotted spatially, we note a clear structure in T4 not present in T5 (Fig. 2,h; T4: left, T5: right). The tail of larger T4 dendrites clearly cluster in the Ventral-Anterior region of Medulla layer 10, a spatial organisation which is not clearly visible in T5 dendrites within Lobula layer 1. This observed patten in the dendrite hull volume is also shared in both total cable length and number of sections within the dendrite tree-graph (Fig. S1). It is interesting to see that each of these size based metrics is highly correlated, illustrating the consistent relationship between size based metrics show in these dendrites

We have shown here that both T4 and T5 dendrites occupy the same mean proportional volume within their differing neuropils. For T4 dendrites however, we see a heavy tailed distribution of dendrite size not present in T5, and a spatial organisation favouring larger regions spanned by the dendritic arbour in the Ventral-Anterior region of Medulla layer 10 which is not apparent in Lobula layer 1.

Dendrite Depth

We have focused thus far on the manner by which T4 and T5 dendrites fill space along the DV and AP axis. We turn next to understanding how individual dendrites occupy space along the remaining depth axis. In order to do so calculate the normalized neuropil layer depth of dendrite nodes (Fig. 3,a; Material and Methods, Surface Fitting, Volume, and Depth Measurement).

We first investigate the depth of the first branching point of individual dendrites (Dendrite root, Fig. 3,b and c; solid lines). We find no meaningfully large mean effect of type ($\eta_p^2 \leq 0.02$). We find a small main effect of subtype ($\eta_p^2 = 0.028, \text{CI}:[0.021, 0.038]$). *Post-hoc* comparisons indicate a small to medium effect size when comparing the a subtype with the c ($\text{Cohen's}_d = -0.377, \text{CI}:[-0.244, -0.377]$) and d ($\text{Cohen's}_d = -0.490, \text{CI}:[-0.429, -0.574]$) subtypes. This indicates that the a subtype in both T4 and T5 starts branching closer to the surface of their neuropil layer in comparison to c and d subtypes. We find no meaningfully large interaction effect between types and subtypes ($\eta_p^2 \leq 0.02$). Qualitatively however, we note that our data seems to indicate that T4 a-b subtype dendrite roots are closer to the Medulla layer 10 surface in comparison to c-d (Fig. 3,b) in a more notable manner than is observed in T5 (Fig. 3,c).

When considering the depth of non-root nodes we find no differences between type, subtype, or interaction ($\eta_p^2 \leq 0.02$). This indicates that individual dendrites, excluding the start of dendritic branching, occupy the same depth within the neuropil layer regardless of type and subtype, or direction of innervation within the neuropil layer itself.

We next consider the manner by with T4 and T5 dendrites project across their respective neuropil layer. As both Medulla layer 10 and Lobula layer 1 are well approximated by a curved surface, two possibilities exist. Either, Dendrites could follow this curvature as they fill space, or they could project across this curvature. By including the euclidean distance from the dendrite root point as a covariate predictor for normalized depth, we find a small main effect ($\beta_p = 0.214, \text{CI}:[0.209, 0.219]$). With no meaningful effect of type or subtype, this tells us that all T4 and T5 dendrites project across the neuropil layer at a slight angle (Fig. 3,d and e), with increasing depth in the

neuropil layer as you move away from the dendrite root. The interaction between normalized euclidean distance from the root and dendrite type (T4, T5) additionally shows a small ($\beta_p = 0.214, \text{CI} : [0.209, 0.219]$). *Post-hoc* comparisons reveal a difference in the slopes between T4 and T5. Here we see that the slope for T4 is marginally less steep than that of T5 ($\Delta\beta_p = -0.088, \text{CI} : [-00.083, -00.092]$, Fig. 3,c, T5; d, T5).

Taken together our analysis shows inconclusive evidence that the depth at which dendrite subtypes begin arborising may differ by subtype, more noticeably for T4 than T5 subtypes. The depth of the dendritic arbour itself, excluding the dendrite root, does not differ between types and subtypes. Finally, we find that these dendrites project across their respective neuropils, rather than growing along the curved space.

Dendrite Initial Positions

Each column within the Medulla and Lobula contains four T4, or T5 dendrites, one of each subtype. With the absence of neuropil specific spatial column information, we investigate the pairwise nearest neighbour relationships between dendrite root nodes. This informs us about any possible spatial structure in the initial starting positions of dendritic arborisation. We find both the subtype specific nearest neighbour pairings for dendrite root nodes, and additionally the global subtype agnostic unique pair assignment which minimises the total distance between pairs of dendrite root nodes (Fig. 4,a; Materials and Methods Dendrite Root Nearest Neighbour Matching). Along side subtype labels, we additionally group data into "same" (e.g a→a), "opposite" (e.g a→b), or "orthogonal" (e.g a→c and a→d) groups.

When looking at the subtype specific distribution of nearest neighbours, we find that in all cases the "opposite" subtype is the closest nearest neighbour for any given dendrites root, and the "same" subtype is always the furthest, with "orthogonal" subtypes occupying the middle distance with no separation between which of the "orthogonal" subtypes is closer (Fig. 4,b). Additionally, we observe that within T4 but not T5 dendrites, the horizontal (a,b; Fig. 4,b i, solid lines) subtypes and vertical (c,d; Fig. 4,bi dashed lines) distributions differ. The vertical subtypes show a greater distance between their nearest neighbours in relation to the horizontal, which is not the case in T5 dendrites (Fig. 4,b ii).

Based on the subtype agnostic nearest neighbour pairing, we can additionally

calculate the probability of a given nearest neighbour being of the "Opposite", "Same" or "Orthogonal" classification (Fig 4,c). We find that in both T4 and T5 the nearest neighbour root node is most likely to be of the "Opposite" classification in a manner which is well above chance. This pattern also extends to subtype-specific pairings (Fig. 4,d). Here, for both T4 and t5 we see that the most probable nearest neighbour is of the opposite subtype (a to b, c to d), and the same subtype the least (Fig. 4,d diagonal), with the orthogonally oriented subtypes positioned between the opposite and same subtypes.

This indicates a clear spatial organisation in the dendrite root node positions, highlighting the potential importance of the initial pattern of innervation before dendritic arborisation. How this result relates to the spatial position of dendrite root nodes within optic lobe columns remains to be determined however.

Dendrite Orientation and Geometry

The asymmetric orientation of T4 and T5 dendrites has been well established [21, 23, 25, 26, 29]. Beyond this orientation however, the high resolution of these data allow for the analysis of the orientation of individual dendritic sections and geometry of bifurcations. Given the observed elliptical shape oriented along the dorsal-ventral axis, we investigate how this impacts the geometry of individual dendrites.

Dendrite Orientation

For each dendrite we can calculate the mean angular orientation of individual sections within the dendrite, which shows a clear organisation into the four known subtypes in both T4 and T5 (Fig. 5, a and b). This dendrite section based analysis of orientation is in line with similar analysis conducted on the orientation of differing Strahler order sections [23].

We next analyse the radial orientation sections within the dendrite. In order to do so we calculate the signed radial angle of each dendrite section [40] (Fig. 5,c; Materials and Methods Geometry Analysis). Given the dominant elongation along the DV axis observed, coupled with four orientations of subtypes, we wish to know if either dendrite sections align with the DV and AP axis, or alternatively, if sections orient radially

outwards from the dendrite root node.

We find a tightly symmetrical distribution of radial section angles with no difference between subtypes (Fig. 5, d (T4) and e (T5)) oriented around $\sim \pm\frac{\pi}{4}$. We note that T5 Dendrites show a broader set of radial orientations than T4, likely caused by growth in differing neuropils and different local spatial constraints. We observe that radial orientation of internal and external segments differ, with internal sections (Fig. 5, d,e; solid lines) showing a tighter radial angle closer to $0°$, more closely aligned with the vector from the dendrite root in comparison to external sections (Fig. 5, d,e; dashed lines).

Although previous work has identified a radial angle distribution centred around $0°$ [40], we find that within T4 and T5 dendrites, sections are still oriented consistently outward from the start of branching, however distributed symmetrically around $0°$ at $\sim \pm\frac{\pi}{4}$. This shows that individual dendrite sections, rather than being oriented along or across the DV or AP axis, are oriented outwards from the initial branching point in a similar manner for both T4 and T5 dendrites as well as their subtypes. We also note that, although still oriented outwards, external sections show a broader distribution and are less constrained by the radial orientation away from the definite root node in comparison to internal sections. This indicates that the manner in which these dendrites orient individual sections, and by extension their asymmetric outgrowth, is to project outwards from the start of dendrite branching in a systematic and conserved manner across subtypes, as opposed to orienting along the DV or AP axis.

Dendrite Bifurcation Geometry

As our next step in building our understanding of the branching structure of T4 and T5 dendrites, we analyse the geometric structure of bifurcations in the dendrite arborisation. Note that we limit our analysis strictly to bifurcations, although some trifurications, or higher are present within the dataset. Additionally, rather than calculate angles based on the whole section between root, branch, and leaf nodes, we limit analysis to $0.1\mu m$ region around the branch node, using the full skeleton reconstruction as opposed to the reduced tree-graph representations (See Materials and Methods, Neurons as Tree Graphs; Geometry Analysis). Each bifurcation is split into three angular components γ and ω, the angles between the parent branch and each of

its two children, and θ the angle between the two child branches (Fig. 5,f). As γ and ω are ordered arbitrarily they are collapsed together for analysis unless otherwise noted.

When first comparing the distributions of these angular components, we find no meaningfully large effects of type, subtype, or their interactions ($\eta_p^2 \leq 0.02$, Fig. 5, g and h). We next compare the pairwise relationships between angular components. When comparing angles γ and ω (Fig. 5.i) the main effects of type, subtype, and interaction are $\eta_p^2 \leq 0.02$. However γ emerges as a strong predictor of ω ($\beta_p = -0.55, \mathrm{CI} : [-0.54, -0.56]$), indicating a clear inverse negative relationship. No such relationship is found when comparing either γ or ω with the child angle θ (Fig. 5,j; all $\eta_p^2 \leq 0.02$ and $\beta_p \leq 0.14$).

We next investigate the planarity of dendritic bifurcations, a property which has been observed in a number of vertebrate neurons [43–45]. Additionally, as the occupied space of T4 and T5 dendrites is naturally flat, we create a simple null model by drawing sets of three unit vectors with a parent vector oriented along the negative x-axis and the two child vectors oriented along the positive x-axis. We additionally scale the distribution of points to align with the average dispersion along each axis observed in our data for T4 and T5 separately, derived from the PC weighting (See Materials and Methods, Geometry Analysis).

First, we look at the sum of angular components for each bifurcation. The sum of angles at a bifurcation in 3D are restricted in three ways, (i) each angle will be smaller than or equal to 180°, (ii) the largest angle will be $\leq$ the sum of the other two, and (iii), the sum will be $\leq 360°$ [43]. The sum of angular components within bifurcations peaks at 2π, with no meaningfully large differences between types, subtypes or interaction ($\eta_p^2 \leq 0.02$). The observed distribution is more heavily dominated by values close to 2π than observed in our random null model (Fig. 5,k).

Second, we compute the Dihedral angle β for each bifurcation, recommended in [43] as a measure of bifurcation flatness (Fig. 5,l insert; Materials and Methods, Geometry Analysis). Again, no meaningfully large difference is found between type, subtype, or interaction ($\eta_p^2 \leq 0.02$). Additionally we note that the observed distribution is more concentrated around π in comparison to our simple random null model.

These taken together, these results indicate that bifurcations within T4 and T5 are identical across both types and subtypes, with individual bifurcations being flatter than

expected by chance and occupying a circular space. The inverse relationship observed between γ and ω is indicative of an optimal spatial embedding whereby both child sections are oriented forward from the parent section and maximally distant from each-other. Due to the summation of angles to 2π the child angle θ then occupies the remainder of the circular space due to the bifurcation planarity.

Dendrite Topology

Our final section of analysis considers the topological and graph-theoretical structure of T4 and T5 dendrites. We focus on describing the underlying nature of the dendritic tree-graph as well as the fundamental properties of edge weights, allowing us to draw inference regarding differing branching and terminal rates in both T4 and T5 dendrites.

Dendrite Graph Structure

We first determine the nature of the underlying tree-graph for T4 and T5 dendrites. At one extreme, a star graph contains a single internal node and all other nodes are external, leaf nodes. For such a graph I, the number of branching nodes is equal to 1. At the other extreme, a full binary tree is a tree-graph whereby all internal nodes have an out degree of two. Within the reduced tree-graphs used here where all nodes with a single parent edge and a single child edge are removed, a full binary tree will have $\frac{n-1}{2}$ internal nodes for n total nodes (see Materials and Methods, Neurons as Tree Graphs). When plotting the relationship between total number of dendrite nodes and total number of branching nodes (Fig. 6,a) we find that all T4 and T5 dendrites are slightly beneath the upper bound of a full binary tree, with no meaningfully large differences between type, subtype and type:subtype ($\eta_p^2 \leq 0.02$).

When observing the out degree distribution of dendrite tree-graphs we see that these dendrites are dominated by nodes with an out degree of 0 (all leaf nodes) and 2 (Bifurcating branch nodes). Interestingly, there is a highly consistent but small number of trifurcations within the dataset. We note that these trifurcations could be a result of the skeletonization process, or alternatively these could be structurally relevant in some manner, potentially as points which minimize total cable length in the manner of Steiner points [47]. We find no meaningfully large differences between types, subtypes

or type:subtype interactions ($\eta_p^2 \leq 0.02$).

We next consider the symmetry of dendrite tree-graphs. Tree asymmetry has long been used as a metric in the analysis of neuron morphology [48–50]. We implement here a weighted tree asymmetry metric, similar to [50] (See Materials and Methods, Branching Structure and Symmetry Quantification). Rather than using a single summary statistic per dendrite, we show the full distribution of scores across a single dendrites, showing the clear symmetric nature of T4 and T5 dendrites (values close to 0 are closer to symmetric, Fig. 6,c). This is in line with previous observations [48, 50, 52] of tree symmetry in neuron morphologies. Again, no meaningfully large differences are found for type, subtype, or type:subtype interactions ($\eta_p^2 \leq 0.02$).

We note that external leaf nodes are distributed through out the tree graph depth (Fig. 6,d), again with no differences observed between type and subtypes ($\eta_p^2 \leq 0.02$). Much like the relationship between total dendrite cable length and dendrite convex hull volume (Fig. S1, c), their is a strong relationship between the total dendrite cable length and the number of individual segments within each dendrite (Fig. 6,e). With the number of segments as a covariate of total cable length we find segment count is a strong predictor of total cable length ($\beta_p = 1.045, \mathrm{CI} : [1.024, 1.066]$). We also find a significant interaction between types ($\beta_p = 1.045, \mathrm{CI} : [1.024, 1.066]$), with the T4 slope being marginally steeper than that of T5 dendrites ($\delta\beta_p = 0.125, \mathrm{CI} : [0.111, 0.139]$).

Together, these results speak towards a highly conserved topological structure for all T4 and T5 dendrites, as well as their subtypes. We fail to find any distinguishable characteristic within this structure which would be in favour of arguing for differences between subtypes mediated by differing orientations, or neuropil specific differences between T4 and T5 with the exception for the slight differences in slopes observed in the relationship between section counts and total cable lengths.

Dendrite Section Lengths

We next turn to investigate any differences in the individual sections between T4 and T5 and their subtypes. Our analysis here includes an additional factor beyond type and subtype, source, which determines the internal or external nature of an individual section (See Materials and Methods, Neurons as Tree Graphs). We first investigate the decay of section lengths as a function of tree depth (Fig. 6,f). We find no meaningfully

large differences between type, subtype, source, or interactions (all $\eta_p^2 \leq 0.02$ and $\beta_p \leq 0.14$). We note however that sections closer to the dendrite root (with lower depth) particularly within internal sections, appear marginally longer before the section lengths stabilise. This observation of an initial decay followed by stabilization has been observed previously in mouse Pukinje cells [53], and in line with optimal wiring and conduction time trade offs which would imply proximal longer runs and distal finer segmentation [42]. T4 internal section length also appear qualitatively greater than T5 across all tree depths (Fig. 4,f; left).

The individual section within out dendrite are a collection of short edges which curve around the individual root, branch and leaf nodes within the tree graph (Fig. 6, g). We would like to understand how much deviation their is from the shortest vector between points as the dendrite section projects between them. As such, we measure for each section the mean angular deviation between individual tree graph edges and the euclidean vector between the source and target point of the section, and the angular variance of the individual edges. We find no differences between types and subtypes ($\eta_p^2 \leq 0.02$), showing the curvature within individual segments is tightly conserved again across types, subtypes, and sources.

We next investigate the distribution of individual section lengths across T4 and T5 and their subtypes. Additionally, in order to account for neuropil specific differences we scale individual dendrites along their Eigen-axis to have equal variance, creating uniform spherical dendrites without changing the topological structure but transforming the individual edge weights (Fig. 7,a and b).

Interestingly, in both original units and scaled datasets, we find no meaningful differences between type, subtype, source, or their interactions ($\eta_p^2 \leq 0.02$). Due to the high skew observed in these data, we also test log-transformed values, which has the same result ($\eta_p^2 \leq 0.02$).

Considering the full dendritic tree as a summation of its individual sections, our analysis here again shows a highly conserved structure with no meaningfully large differences between T4 and T5 dendrites and their subtypes.

Section Weight Distributions

Previously, measures of dendrite and axon section lengths have been observed generally with a range of right-skewed distributions [50, 54–58]. However, understanding the specific nature of the observed right-skewed distribution tells us something of the underlying mechanistic process. For example, models of multiplicative dynamics have been shown to directly give rise to the observed log-normal distribution of spine size in the auditory cortex of mice [58].

In order to better understand the specific distributions observed here, we perform an exploratory analysis in order to determine which from a set of six distributions best fits the observed section length data. We choose to compare exponential, log-normal, gamma, Wald, log-logistic, and Weibull distributions. Although we note that an exponential distribution is a special case of the gamma distribution with $k = 1$, we keep the two distributions distinct for clarity. Each of these distributions is an example of a right-skewed distribution, and can be related to differing generative processes. We fit all six distributions to each type, subtypes, and source combination for both raw and variance scaled section length data. Distributions are compared using the Bayesian Information Criterion (BIC) and out-of-sample assessment using cross-validation.

Within all groups, internal section length distributions are consistently best fit by a gamma distribution (Fig.7 c,d; Supplementary Figure 2 and 3). Alternatively, External section lengths are, in all cases, best fit by a log-normal distribution (Fig.8 e,f; Supplementary Figure 2 and 3). Although we found no differences between types and subtypes, it is notable that the best fitting distribution for the differing section types (internal and external) differ. Although both are commonly used distributions, they highlight two different types of process.

In the case of internal section length, one logical mechanism which gives rise to the observed gamma distribution relates to a process involving the necessity for multiple events to occur before a branching event takes place. Giving a more concrete example, this implies that a branching event will occur during growth after n sub-events, which are exponentially distributed, have first occurred [59]

In comparison, a log-normal distribution observed here in external section lengths has been previously related to dendrite spine outgrowth and lengths [58], as well as

axonal tree section lengths [50]. The log-normal distribution is a result of a central-limit theorem like process resulting from the product, rather than the sum, of multiple samples [60, 61].

Together, this explorative analysis indicates fundamentally differing generative processes underlying branching rates and termination rates. However, the lack of differences observed within our data, and shared best fitting distribution across groupings in our analysis, indicates that this process is equivalent across T4 and T5, as well as subtypes.

Discussion

By leveraging the high resolution morphological data available through new EM reconstructions of all T4 and T5 dendrites we are able to offer a quantitative characterisations of the similarities and differences between T4 and T5 dendrites, as well as their subtypes at a level not available through typical imaging techniques.

Dendrite Structure is Homogenous across Types and Subtypes

The T4 and T5 dendrites are characterised by their distinct, subtype specific, directional asymmetry [22]. One may assume that this would lead to morphological differences within the dendrite branching structure. We, however, observe consistent homogeneity in all geometric, and graph-theoretical measures across all T4 and T5 dendrites, as well as their subtypes.

The dendrites of T4 and T5 neurons, and their subtypes, are all well characterised by the same close to binary and symmetric tree-graph with little variability across both neuropils and subtypes. Interestingly, the deviation from a binary tree manifests in a small but consistent proportion of trifurcations. Their consistency leads us to believe that they are less likely to be a direct result of the sketonization procedure. This may indicate that they are biologically meaningful, for example being Steiner points which minimize the total dendrite cable [47], however further analysis is needed in order to determine if this is the case.

We also observe a striking similarity in the geometry of dendritic branching. This indicates that the branching mechanism within these dendrites is conserved across types

and subtypes. Interestingly, the flatness and angular distributions observed indicate a simple rule whereby the two child sections are maximally separated from each other. This is due to the relative planarity of these bifurcations, coupled with the negative correlation between both parent and child branching angles. This maximal partitioning may relate to self-avoidance mechanisms, as well as optimal spatial embedding.

That we observe flatter bifurcations than would be expected by our random null model indicates that this is not simply a result of the narrow depth of Medulla layer 10 and Lobula layer 1, but rather a result of additional constraints on branching geometry. The flatness of dendrite bifurcations has been previously related with both the stochastic process of connecting to the closest point in space randomly [46], and being an emergent property of the local 3D elastic tensions in neurites, where distal parts of branches develop force equilibrium when anchored to the substrate [43].

These dendrites also show similar spatial occupancy, shown in their elliptical structure and consistent elongation along the Dorsal-Ventral axis regardless of subtype, as well as neuropil layer depth innervation. Once appropriate scaling is applied, the mean volume of these dendrites additionally does not differ, in line with the importance of the spatial occupancy of ~ 7 columns and necessities of motion detection to integrate across multiple adjacent visual points [25, 26].

Spatial Occupancy Differs Between Neuropils

Although the structure of individual dendrites is highly conserved across types and subtypes, we observe some small yet insightful differences between neuropils and subtypes in terms of their spatial occupancy and initial arborisation positions. Of particular interest is the differing distribution shape and spacial organisation in all size based metrics. Specifically, the population of T4 dendrites shows a heavy tail not present in the comparably symmetric T5 distribution. The tail of larger T4 dendrites is focused within the Ventral-Anterior region of Medulla layer 10. It has been previously observed that within the compound eye, across *Drosophilidae* species, larger lenses are present within the Ventral - Anterior region [37–39]. The observed spatial distribution of T4 dendrites could be indicative of a similar pattern being conserved in Medulla columns but not within Lobula columns. In order to investigate this hypothesis however

additional analysis is needed which includes the spatial density of synapses, and neuropil specific spatial column annotations.

We also observe a subtype, but not type, specific relationship in the extent of dendrite innervation along the dorsal-ventral (DV) and anterior-posterior (AP) axis. Vertical (c,d) subtypes show a greater elongation along the DV axis, and narrower width along the AP axis, a trend which is reversed within the horizontal (a,b) subtypes. Interestingly however, the difference between elongation along the DV and AP axis is negatively correlated, indicating that as each dendrite extends along the DV axis, it extends less along the AP axis proportionally. This could be evidence of a cost-constrained mechanism limiting the total size of dendrites, coupled with dominant, subtype specific, elongation along the DV axis.

We also observe differences between horizontal and vertical subtypes in terms of the dendritic root position. Our analysis of dendrite root depths in inconclusive, however there is some limited evidence that horizontal T4 subtypes start branching closer to the layer boundary in comparison to T4 horizontal subtypes, a trend which is not clear in T5 dendrites. In addition to this, we see a clear difference between nearest neighbour partner in T4 horizontal and vertical subtypes when considering oppositely oriented nearest neighbours, whereby horizontal subtypes are closer nearest neighbours than vertical. This trend is not present in T5 neurons.

Together, these results show subtle differences in terms of the spatial occupancy, and innervation structure, between T4 and T5, highlighting important differences between growth in the Medulla and Lobula which is independent of the underlying structure of these dendrites.

Insights into Development

The development of T4 and T5 dendrites, specifically the origin of their characteristic asymmetry remains poorly understood. Although these data originate from a single adult, and as such are a single snapshot of a single adult time point, our analysis has a number of implications to the development of these dendrites.

Our analysis indicates that regardless of the subtype specific orientation of these dendrites, arborisations fill space in a similar manner. As the geometry of dendrite

branching, as well as underlying tree-graph structure is indistinguishable between subtypes, it seems more likely that dendritic development is mediated by the same algorithm across types and subtypes, than differing algorithms are employed and then dendrites are tightly reconfigured at later stages of development in order to achieve this homogeneity.

Our exploratory distribution fitting analysis offers some insight into the likely nature of this developmental algorithm. We first observe a gamma distribution for internal section lengths. When branching is treated as a Poisson process, and multiple events are required before a stable branch occurs, we would expect to observe a gamma distribution as a result [62]. Empirically fit models which treat branching in this manner have previously been used to accurately capture the observed distribution in real data [63–65]. This assumes a stable dendrite branch requires some number of molecular sub events before formation. Actin nucleation, specifically transient, localized Arp2/3 recruitment precedes branch formation in *Drosophila* DA neurons [66], as an example of one such potential molecular sub-event. Further, microtubules have been shown to transiently invade branch precursors, providing a pathway for additional material required for stabilization, initiating changes in dendrite spine morphology [67]. MAP2c in cultured hippocampal neurons has also been shown to promote stabilization of neurites, through the coupling of F-actin and microtubules, consolidating stabilization [68]. Our data is indicative of a complex multi-event mechanism which govern branching within these dendrites

The log-normal distribution observed in dendrite terminal sections however points to a simpler process. Log-normal distributions come about through multiplicative mechanisms [60, 61]. Dendrite spine lengths have previously been observed to follow this type of distribution, both experimentally and within models [3, 58, 69]. How this may relate mechanistically to the outgrowth of dendrite external sections is not as clear however. Live imaging has shown stochastic switching between growth, paused, and shrinking states in an episodic manner within dendrite tips [41]. This state switching coupled with current section resources, could in principle generate the multiplicative effect required for the observed log-normal distribution [50].

Previous work has also characterised the innervation pattern of T4 and T5 dendrites during neuropil innervation, but before dendrite outgrowth [27]. This work illustrates

that T4 and T5 dendrites innervate along the AP axis in a temporal-spatial wave, and that dendrites from the same neuroblast occupy the same spatial regions. This compliments our analysis showing the nearest neighbour relationships in T4 and T5 dendrite root nodes. Further, our analysis highlights the seemingly tightly controlled subtype specific spatial patterning of T4 and T5 dendrites at the point of neuropil innervation. By extension, these nearest neighbour relationships mediate which dendrites are developing adjacently within the same spatial regions. This subtype specific structure may be indicative of tightly controlled initial conditions and spatial organisation which preseed dendritic outgrowth and the emergence of their characteristic asymmetry.

Finally, given the previously documented spatial synaptic compartmentalisation present on both T4 and T5 dendrites [25], our observation of dendritic projections across not along their respective neuropil layers offers a simple hypothesis. Specifically, the compartmental spatial organisation of synapses onto these dendrites may, in part, be a simple result of the spatial availability of input partners in a stratified manner within the local environment whereby input partners are separated by their depth within the neuropil layer.

Future Analysis and Perspectives

Multiple avenues of future work open up in order to better understand the morphological structure of T4 and T5 dendrites from connectomics data. The most obvious is to investigate comparative differences in T4 and T5 between datasets, utilising the available Male optic lobe connectome which has been recently released [13]. This would allow us to better capture variability across individuals, and also allow for sex specific comparisons relating to differing size, shape, and orientation of *Drosophila* compound eyes between males and females across species [38].

Second, it is important to understand the synaptic distributions and columnar relationships in T4 and T5. Synaptic inputs are vital to dendritic development [70–72]. Further, the origin of the distinct spatial compartmentalisation of synapses onto T4 and T5 dendrites is not well understood, however we propose a simple hypothesis here. Extending our analysis to included synaptic, columnar, and by extension, visual space,

would prove insightful, however see [23, 73] for analysis of T4 and T5 neurons which includes visual space mapping.

With the wealth of available data, generative, data-driven models of T4 and T5 dendrite morphology are within reach. Our results indicate that the implementation of such models may be possible without the use of fundamentally different rules, or a differing algorithm, between T4 and T5 and their subtypes. Such modelling approaches would be able to shed light on the developmental algorithm employed in a manner which quantitative analysis of the data cannot.

Limitations

The data presented here is from a single adult female *drosophila*, offering a view of a single snapshot of T4 and T5 dendrite morphology. Although thought of as complete, and offering a new gold standard in data quality, some noise is undoubtedly introduced from the complex processing steps needed to generate a usable dataset from the EM image stack. We ensure that all dendrites are labelled as complete within the FLYWIRE dataset, as well as manually verify the accuracy of dendrite annotation. However, particularly small branches are likely missing from the morphological reconstructions of neurons. We argue that as this error is likely missing at random, and the n of T4 and T5 neurons is sufficiently large, this error rate is likely uniform across the dataset and would not change any of our findings. As these data also come from a single *drosophila*, it is also possible that different individuals show differing results. Given the fundamental nature of T4 and T5 neurons in early visual processing and motion detection, we feel this is unlikely to be the case. The question of individual variability between datasets is an intriguing one which requires further work and comparative analysis between datasets in order to be fully understood.

Conclusions

In summary, we show that the underlying structure of T4 and T5 dendrites, as well as their subtypes, is indistinguishable. There are however, some important type and subtype specific differences in the manner of spatial occupancy and initial dendritic branching. With this detailed characterisation of T4 and T5 dendritic morphology, and

given the observed homogeneity, we reason that the underlying developmental algorithm is likely conserved across all T4 and T5, and their subtypes. However, this also indicates that the characteristic asymmetry of these dendrites is not a result of fundamentally different developmental processes, and as such the mechanism for this remains illusive.

Materials and methods

Data and Code Availability

Flywire neuron ids and types are published with [9]. Specific neuron IDs used within this manuscript, as well as type and subtype annotations are available in Supplementary file 1. The open source Python toolboxes "fafbseg" [74] and "skeletor" [75] were used to obtain and skeletonize neuron meshes. All further analysis and plots were generated with custom python code and toolboxes. Analysis code and data used will be made available with submission.

T4 and T5 Neuron Morphologies

The complete Flywire dataset comprises of ~ 130000 annotated neurons, proofread and annotated by an extensive community of researchers and citizen scientists [7, 8, 76]. The optic lobe specific dataset has been published previously in [9], which provides the annotations for reconstructions used within this study. A total of 5919 T4/T5 neurons have been identified within the dataset, and 5653 individual dendrites were accurately extracted for analysis. Supplementary Table 1 gives counts by subtype for available and included dendrites. All reconstructions have been annotated as complete within the FLYWIRE dataset. After skeletonization, all neurons are converted to μm from nm, and resampled to $0.1\mu m$.

Neurons as Tree Graphs

Skeletons were extracted with the wavefront algorithm [75], and each skeleton is a tree-graph representation of a neuron. Each tree-graph is rooted at the soma, in the case of complete neurons, or the first common ancestor of nodes within the dendritic sub-tree (referred to as the dendrite root node), and all edges are oriented away from

the root node. For completeness, we provide a brief overview of graph-theory specific to directed tree-graphs here and the components relevant to this manuscript.

A neuron is modelled as a directed tree:

$$T = (V, E, r), \qquad r \in V \subset \mathbb{R}^3, \tag{1}$$

where V is the set of 3-D coordinates defined by the skeletonization algorithm and $E \subset V \times V$ the set of oriented edges. r denotes the root node of the tree. $e = (u \to v)$ denotes an edge from u to v, where u is the source node, and v the target.

Each edge carries the Euclidean length $w(e) = \|v - u\|_2$. The tree weight (total cable length) is:

$$W(T) = \sum_{e \in E} w(e). \tag{2}$$

For $v \in V$:

$$\begin{aligned} \deg^+(v) &= |\{(v, w) \in E\}|, \\ \deg^-(v) &= |\{(u, v) \in E\}|, \\ \deg(v) &= \deg^+(v) + \deg^-(v). \end{aligned} \tag{3}$$

Where $\deg^+$ denotes the out-degree of a node, $\deg^-$ denotes the in-degree, and $\deg(v)$ the total degree. As edges point away from the root, $\deg^-(r) = 0$, and $\deg^-(v) = 1$ for every $v \neq r$. branch nodes have $\deg^+ \geq 2$ and leaf nodes $\deg^+ = 0$. An edge is *external* if e_v is a leaf, otherwise *internal*.

For any two nodes $u, v \in V$ there exists a unique undirected path

$$P_V(u, v) = (v_0 = u,\ v_1, \ldots, v_k = v), \tag{4}$$

with $k = d(u, v)$ steps.

The corresponding edge sequence:

$$\begin{aligned} P_E(u, v) &= \big(e_0, e_1, \ldots, e_{k-1}\big), \\ e_i &= (v_i \to v_{i+1}) \text{ or } (v_{i+1} \to v_i), \end{aligned} \tag{5}$$

lists the k oriented edges traversed in order; note that orientation may be reversed relative to E when the walk proceeds toward the root.

Unweighted and weighted path lengths are

$$
\begin{aligned}
d(u,v) &= k, \\
d_w(u,v) &= \sum_{i=0}^{k-1} w(e_i).
\end{aligned}
\tag{6}
$$

Node depth is its unweighted distance to the root, $h(v) = d_w(r,v)$, and an edge inherits the depth of its distal node.

Every maximal path of intermediate nodes with $\deg^+(v) = \deg^-(v) = 1$ is contracted into a single edge whose weight is the sum of the collapsed weights. The reduced graph is $T_r = (V_r, E_r)$. Such reduced trees dramatically minimise the number of nodes and edges within each neuron skeleton.

For any node $v \in V$ we define the *subtree* rooted at v as:

$$
\begin{aligned}
T_v \;&:=\; (V_v, E_v), \\
V_v &= \{\, x \in V \mid v \preceq x \,\}, \\
E_v &= \{\, (y \to z) \in E \mid y, z \in V_v \,\},
\end{aligned}
\tag{7}
$$

where $v \preceq x$ means that v lies on the unique root–to–x directed path in T. Thus T_v contains v and all its descendants together with the edges that connect them, and is itself a rooted, oriented tree with root v.

Branching Structure and Symmetry Quantification

Considering a tree graph with no nodes where $\deg^+ = \deg^- = 1$, as is the case for the reduced neuron skeleton graphs used here, let $n = |V|$ and L be the number of leaves. Internal node number $I = n - L$. As (i) a *star* tree has one branch point and $L = n - 1$, and (ii) a *full binary* tree satisfies $L = I + 1$, hence $I = (n-1)/2$, thus for any tree graph we have an upper bound:

$$
1 \;\le\; I \;\le\; \frac{n-1}{2}, \tag{8}
$$

This provides limits between maximally condensed and maximally branching tree-graphs, and no tree-graph can exist outside of these bounds. The closer I is to

$(n-1)/2$, the closer to a full binary tree.

Tree asymmetry for a single node, A_v, as defined in [48, 49], is extended similarly to [50] in order to weight the metric by the weight of the sub-tree defined at v with $k \geq 2$ child nodes. In the case of $\deg^+(v) > 2$, we use a mean of all child pairs (p, q):

$$A_v = \frac{1}{\binom{k}{2}} \sum_{1 \leq p < q \leq k} \Big(\frac{|L(T_p) - L(T_q)|}{(L(T_p) + L(T_q) - 1} \cdot \frac{W(T_p) + W(T_q)}{W(T)} \Big), \tag{9}$$

A_v lies in $[0, 1]$, where 0 indicates full symmetry in the branching structure.

Dendrite Extraction and Data Pre-processing

We use a semi-automated method in order to annotate neuron dendrites. We first manually verify the correct rooting of each neuron tree graph at the soma. We then identify the subtree in T which maximises the number of leaves within the subtree whilst minimizing the sum of edge weights using a simple metric, Φ:

$$\Phi^{\max} \; = \; \max_{v \in \mathcal{B}} \Big[\big(1 - \tfrac{W(T_v)}{W(T)}\big) \; + \; \tfrac{L_v}{L} \Big] \tag{10}$$

Where $\mathcal{B}$ si the set of branch nodes within T. Although often the identified subtree will be the dendrite within T4 and T5 neurons, due to either routing errors resulting from the surface mesh and skeletonization procedure, or instances where no single node isolates the root of the dendritic subtree, a further manual step is needed using a custom made GUI. Each neuron dendrite is manually verified as being the complete dendritic subtree. In cases where this is not identified accurately as described above, the reviewer has the ability to manually isolate the dendrite where possible by annotating a single chose node. Dendrites which cannot be completely isolated are excluded from analysis.

Alignment and Scaling

In order to globally align the T4 and T5 dendrite populations, we need to define a suitable shared space for both populations. Taking the 3D point cloud of dendrite tree-graph nodes we first set the origin of the coordinate system to be the centre of a fitted sphere, separately for each population, before aligning the primary eigen axis to the polar spherical axis, or y-axis and the secondary eigen-axis with the equatorial axis,

or the y-axis. Using the column assignments available in FLYWIRE, we find example dorsal, ventral, anterior and posterior columns (Fig. 1,d, insert). We then rotate the population point cloud in a manner which aligns with the Dorsal / Ventral and Anterior / Posterior axis in the column space, preserving the initial eigen-axis alignment. This results in all T4 and T5 dendrites being aligned so that the y-axis follows the Dorsal - Ventral axis and x-axis the Anterior-Posterior.

We use a similar procedure to align all dendrites of a single subtype. When aligning individual dendrites, we calculate the covariance matrix using a robust M-estimation procedure based on a Huber-type influence function. This is done in order to minimise the influence of node outliers on eigenvectors, as single long outreaching sections may impact the eigenvector orientation within single dendrites. After Eigendecomposition of the covariance matrix, eigenvectors are aligned similarly to the global procedure so the primary eigen-axis aligns with the y-axis, the secondary eigen-axis to the x-axis and the third to the z-axis. Before calculating angles of rotation we ensure that each eigenvector is oriented along it's positive target basis vector, in order to minimise rotation.

In order to scale point node positions we scale coordinates along their Eigenbasis by s. In the case of Fig. 2.a, s is a constant defined as $1/(\mu + 3\sigma)$ where μ is the population mean of the highest eigenvalue (λ_1) and σ the population standard deviation of λ_1. This scales all dendrites along each axis to $1 = \mu_{\lambda_1} + 3\sigma_{\lambda_1}$. Alternatively, for unit variance scaling s is a vector equal to $1/\text{var}[e_i]$ where $\text{var}[e_i]$ is the variance along each eigenvector, e. This scales dendrite to have equal variance along each axis.

Surface Fitting, Volume, and Depth Measurement

In order to find the spanning volume of single dendrites, a convex hull is fit to the node coordinates of each dendrite using scipy.spatial.ConvexHull [77]. We reconstruct surfaces meshes of M10 and L1 via voxelization and marching cubes of all node coordinates in T4 (Medulla layer 10) or T5 (Lobula layer 1) dendrites. Step by step, we first compute the Axis-aligned bounding box for the given point cloud, extended by a fixed padding factor ($2\mu m$) to ensure a spatial margin. This is then discretized into $2\mu m^3$ voxels and each point is assigned to a voxel. 2 iterations of morphological dilation are applied in order to fill small gaps in the set of occupied voxels, and then unoccupied

voxels are removed, retaining only the largest connected region of voxels. This binary grid is then converted to a continuous surface using the marching cubes algorithm as implemented in scikit-image. The resulting mesh is then cleaned by removing unreferenced nodes, duplicated or degenerate faces, filling holes in the mesh surface, and correcting face normals to ensure they are outwardly oriented. Surface meshes are smoothed using the Windowed Sinc method and a band pass filter with a width of $0.01\mu m$, as implemented in [78].

In order to calculate the local depth of a point within each layer mesh we first define an inner and outer surface to the mesh, relative to the origin of the global coordinate space. This is done by sub-setting mesh face normals based on the dot product of their normals and a vector from the coordinate origin to the face centre. Faces with values ≥ 0.3 are treated as belonging to the outer mesh surface, and values ≤ -0.3 as the inner surface. A KDTree is calculated for both the inner and outer surface. For any given point, the nearest neighbour distance is calculated to both surfaces. We then calculate a normalized distance for the point from the inner surface. As T5 dendrites innervate Lobula layer 1 from the opposite side of curvature in comparison to T4 dendrites innervating Medula layer 10, we invert T5 depths. Depth is calculated as follows:

$$d_{norm} = \begin{cases} \frac{d_{inner}}{d_{inner}+d_{outer}} & ,T4 \\ 1 - \frac{d_{inner}}{d_{inner}+d_{outer}} & ,T5 \end{cases} \tag{11}$$

Dendrite Root Nearest Neighbour Matching.

In order to identify dendrite root position nearest neighbours we first assign subtype specific nearest neighbours using KDTrees within each type - subtype combination in order to identify the distance between each T4a, for example, and the closest T4a (not including itself), T4b, T4c, and T4d dendrite root.

In order to determine the probability of a nearest neighbour being of either a specific classification (”opposite”, ”same”, or ”orthogonal”), or specific subtype, we calculate the pairwise distance matrix globally within all T4 and all T5 dendrite root positions separately, and then find the unique pairwise nearest neighbour mapping using the modified Jonker-Volgenant algorithm with no initialisation as implemented in [77].

Geometry Analysis.

When calculating angles between vectors in $\mathbb{R}^3$ we project vectors $[v_1, v_2]$ to the plane orthogonal to the normal vector, n, by taking the rejection of each vector from n:

$$v_i^{\perp} = v_i - \frac{v_i \cdot n}{||n||^2} n \tag{12}$$

We then calculate the signed angle, θ, between v_1 and v_2 in the plane as:

$$\theta = \text{atan2}((v_1^{\perp} \times v_2^{\perp}) \cdot \hat{n}, v_1^{\perp} \cdot v_2^{\perp}) \tag{13}$$

Where $\hat{n}$ is the unit normal of the basis vector, $v_1^{\perp} \cdot v_2^{\perp}$ is the cosine of the angle. $(v_1^{\perp} \times v_2^{\perp}) \cdot \hat{n}$ gives the signed sine, where the sign is determined by the right hand rule with respect to n. $\text{atan2}(y, x)$ returns the signed angle $\theta \in (-\pi, \pi]$.

As defined in [79], the circular mean is calculated as:

$$\bar{\theta} = \left(\sum_{i=1}^{n} \cos\theta_i, \sum_{i=1}^{n} \sin\theta_i \right). \tag{14}$$

and Variance as:

$$V = \sqrt{\left(\sum_{i=1}^{n} \cos\theta_i \right)^2 + \left(\sum_{i=1}^{n} \sin\theta_i \right)^2}. \tag{15}$$

The Dihedral angle β, is the "the angle between the daughters' half-plane and the plane formed by the parent segment and the line perpendicular to daughters' bisection through the bifurcation point in the daughters' plane" [43] (Fig. 5,l, insert). In order to calculate this for a set of parent and two child vectors $[p, c_1, c_2]$ centred on their branching point, we first find the bisector, b, of c_1 and c_2 as:

$$b = \frac{v_1/||v_1|| + v_2/||v_2||}{||v_1/||v_1|| + v_2/||v_2||||}. \tag{16}$$

We then calculate the angle between b and p from the perspective of the plane

defined by the normal vector, n, given by:

$$\mathbf{n} = (\mathbf{c}_1 \times \mathbf{c}_2) \times \mathbf{b} \tag{17}$$

This results in the Dihedral angle β which is between 0 and π. At both extremes, this value represents vectors sitting on the same plane, however at 0 child vectors are on the plane oriented in the same direction as the parent relative to the bifurcation points, and at π they will be oriented away.

In order to generate bifurcation random null-models we randomly generate $1,000,000$ sets of three 3-dimensional unit vectors. We ensure that one vector is oriented towards the negative x-axis to represent the parent section, and the other two are oriented along the positive x-axis. This ensures an approximation of the outward facing branching structure observed. Second, sets of bifurcation vectors are then scaled along their z-axis separately for T4 and T5 by the cube root of the mean variance explained by the third principle component, in order to mimic the natural flatness of the occupied space of T4 and T5 dendrites.

Explorative Distribution Modelling

We divide dendrite populations by type (T4, T5), subtype (a,b,c,d) and section type (internal, external). We then fit using maximum likelihood, for each group, six test distributions in order to compare goodness of fit. The distributions and log-likelihoods are as follows:

Wald (Inverse Gaussian) Distribution, with mean $\mu > 0$ and shape $\lambda > 0$:

$$f(x|\mu, \lambda) = \sqrt{\frac{\lambda}{2\pi x^3}} \exp\left(-\frac{\lambda(x-\mu)^2}{2\mu^2 x}\right), x > 0. \tag{18}$$

The Log-likelihood for a sample $\{x_i\}_{i=1}^n$:

$$\ell(\mu, \lambda) = \sum_{i=1}^{n} \left[\frac{1}{2}(\ln\lambda - \ln(2\pi) - 3\ln x_i) - \frac{\lambda(x_i-\mu)^2}{2\mu^2 x_i}\right]. \tag{19}$$

Log-normal Distribution, with log-mean $\mu \in \mathbb{R}$ and log-standard deviation $\sigma > 0$:

$$f(x|\mu,\sigma) = \frac{1}{x\sigma\sqrt{2\pi}} \exp\left(-\frac{(\ln x - \mu)^2}{2\sigma^2}\right), x > 0. \tag{20}$$

$$\ell(\mu,\sigma) = \sum_{i=1}^{n} \left[-\ln x_i - \ln(\sigma\sqrt{2\pi}) - \frac{(\ln x_i - \mu)^2}{2\sigma^2}\right]. \tag{21}$$

Gamma Distribution, with shape $k > 0$ and scale $\theta > 0$:

$$f(x|k,\theta) = \frac{x^{k-1}e^{-x/\theta}}{\Gamma(k)\theta^k}, x > 0. \tag{22}$$

$$\ell(k,\theta) = \sum_{i=1}^{n} [(k-1)\ln x_i - x_i/\theta] - n(k\ln\theta + \ln\Gamma(k)) \tag{23}$$

where Γ is the gamma function.

Exponential Distribution (Gamma distribution special case with $k = 1$) with scale $\theta > 0$:

$$f(x|\theta) = \frac{1}{\theta}e^{-x/\theta}, x \geq 0. \tag{24}$$

$$\ell(\theta) = -n\ln\theta - \frac{1}{\theta}\sum_{i=1}^{n} x_i. \tag{25}$$

Log-logistic Distribution with shape $c > 0$ and scale $s > 0$:

$$f(x|c,s) = \frac{c}{s}\left(\frac{x}{s}\right)^{c-1}\left(1 + \left(\frac{x}{s}\right)^c\right)^{-2}, x > 0. \tag{26}$$

$$\ell(c,s) = \sum_{i=1}^{n} \left[\ln(c/s) + (c-1)\ln(x_i/s) - 2\ln(1 + (x_i/s)^c)\right]. \tag{27}$$

Weibull Distribution (minimum) with shape $c > 0$ and scale $\lambda > 0$:

$$f(x|c,\lambda) = \frac{c}{\lambda}\left(\frac{x}{\lambda}\right)^{c-1} \exp\left[-\left(\frac{x}{\lambda}\right)^c\right], x \geq 0 \tag{28}$$

$$\ell(c,\lambda) = \sum_{i=1}^{n} [\ln(c/\lambda) + (c-1)\ln(x_i/\lambda) - (x_i/\lambda)^c] \tag{29}$$

For each fitted distribution we calculate the Bayesian Information Criterion (BIC) as:

$$\mathrm{BIC} = k \ln n - 2\ell(\hat{\theta}) \tag{30}$$

where k is the number of free parameters (2 for Wald, log-normal, gamma, log-logistic, and Weibull Distributions; 1 for exponential). n is the number of observations within the sample and $\ell(\hat{\theta})$ is the maximised log-likelihood. Lower BIC indicates a better trade off between model fit and parsimony.

In order to additionally assess the predictive performance of fitted models independent of parametric penalties, we perform K-fold cross-validation within groups. The data were partitioned into $K = 10$ folds, without mixing observations from individual neurons in order to avoid leakage. For fold f, parameters $\hat{\theta}^{(-f)}$ were estimated on the $K - 1$ training folds and evaluated on the held out fold by the predictive log-likelihood per observation:

$$\bar{\ell}_f = \frac{1}{|D_f|} \sum_{x \in D_f} \log f(x|\hat{\theta}^{(-f)}). \tag{31}$$

We report the mean across folds, $\bar{\ell}_{\mathrm{CV}} = \frac{1}{K} \sum_{f=1}^{K} \bar{\ell} f$, as the primary out of sample score (higher is better), together with a 95% confidence interval based on the fold-to-fold standard deviation. Distributions were ranked within each group by $\bar{\ell}_{\mathrm{CV}}$ alongside BIC ranks.

Statistical Analysis

We test for type (T4, T5) and subtype (a,b,c, and d) effects on different measured variables using ordinary least squares (OLS) regression and factorial analysis of variance (ANOVA). Models are fit with a full factorial structure, and sum of squares were evaluated using Type III tests. In cases where an additional continuous covariate is needed, this framework easily extends to factorial analysis of covariance (ANCOVA). We additionally, for each effect (main effects and interaction terms), calculate the partial eta-squared (η_p^2) as an effect size:

$$\eta_p^2 = \frac{\mathrm{SS}_{effect}}{\mathrm{SS}_{effect} + \mathrm{SS}_{error}} \tag{32}$$

where SS is the sum of squares. For continuous effects, standardised β's are used,

obtained from the regression model. We additionally obtain, for each effect size, a non-parametric confidence interval obtained through stratified bootstrap resampling (1000 samples). *Post-hoc* pairwise comparisons were conducted on marginal means, both at the main effect level and within interactions, and Cohen's d was calculated for effect sizes:

$$\text{Cohen}'\text{s}_d = \frac{\mu_i - \mu_j}{\sqrt{(\sigma_i^2 + \sigma_j^2)/2}} \tag{33}$$

where μ represents the group mean and $sigma$ the group standard deviation. Again, non-parametric confidence intervals using 1000 bootstrap resamples are calculated.

Plotting Conventions.

We make liberal use of the empirical probability mass functions (epmf) for plotting distributions throughout, without smoothing. To allow for comparison within plots, binning along the x-axis is the same for all epmf's shown within a plot. Bin counts and ranges are adjusted manually. Error bars are presented in two forms, as specified in a plot by plot basis. In cases where a single observation is available per individual dendrite, a bootstrapped confidence interval around the mean in each bin is shown. Alternatively, when a repeated measure is available within each dendrite, a single epmf is generated for each individual neuron and in order to give an idea of individual variability across the population, error bars show an asymmetrical median absolute deviation (aMAD) to illustrate variance in each bin across neurons. An Asymmetric MAD allows for the possibility that individual variability within each bin is skewed, and can be shown within the plot. aMAD generates a lower and upper bound of variability as:

$$\begin{aligned} \text{MAD}_{\text{low}} &= \text{median}\left(|x_i - \tilde{x}| \mid x_i < \tilde{x}\right) \\ \text{MAD}_{\text{high}} &= \text{median}\left(|x_i - \tilde{x}| \mid x_i > \tilde{x}\right) \end{aligned} \tag{34}$$

where $\tilde{x}$ is the median within the respective bin.

Figures

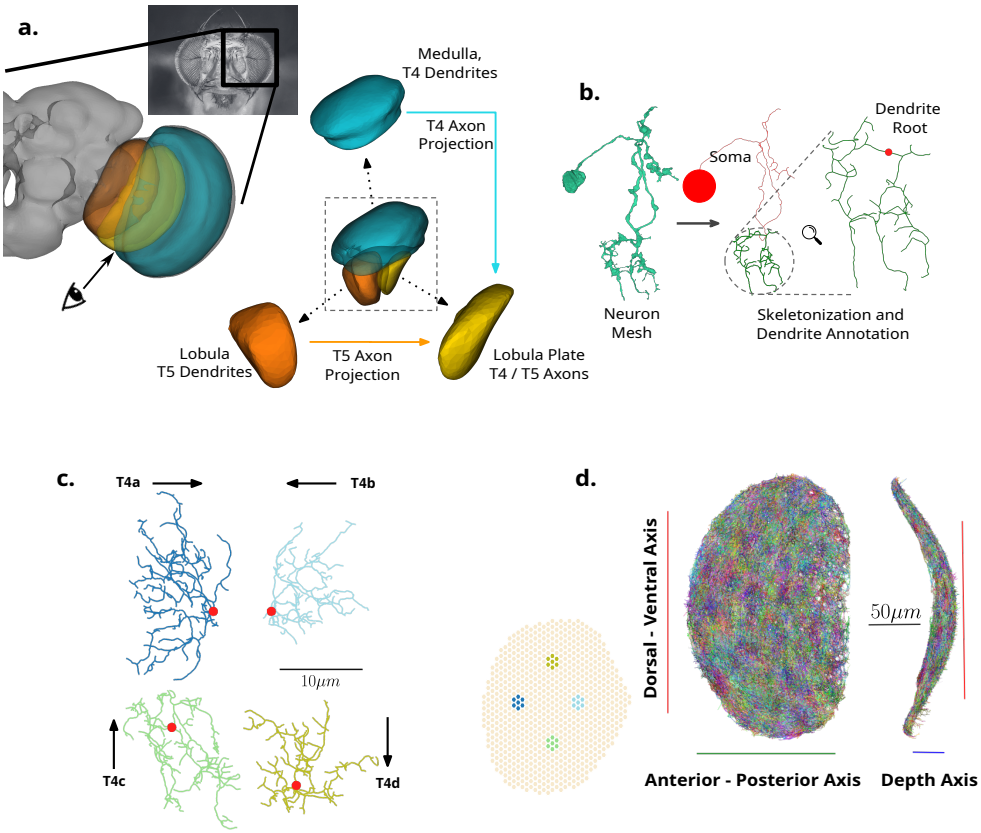

Fig 1. Overview of *Drosophila* optic lobe and T4 / T5 dendrites a) (*left*) View of the right Optic lobe available in FLYWIRE, with Medulla (Turquoise), Lobula (Orange) and Lobula Plate (Yellow) shown. (*right*) Exploded view of neuropils coloured from perspective illustrated in *left*. Coloured arrows denote axonal projections for T4 (Medulla to Lobula Plate) and T5 (Lobula to Lobula Plate). b) Illustration of skeletonization and Dendrite annotation procedure from mesh to extracted example dendrite. c) Example extracted T4 dendrites for each subtype. Red points show dendrite root points (first branching point). Arrows show encoded directional tuning of each subtype, inverse to the direction of dendrite outgrowth. d) All extracted T4 dendrites in the globally aligned Dorsal-Ventral (DV) / Anterior-Posterior (AP) view (*left*) and DV / Depth view (*right*). Insert shows visual column map available in FLYWIRE. Coloured hexagons illustrate Dorsal, Ventral, Anterior, and Posterior example columns used for alignment. Each example dendrite in c matches by colour the T4 dendrite assigned to the centre of each group of coloured hexagons.

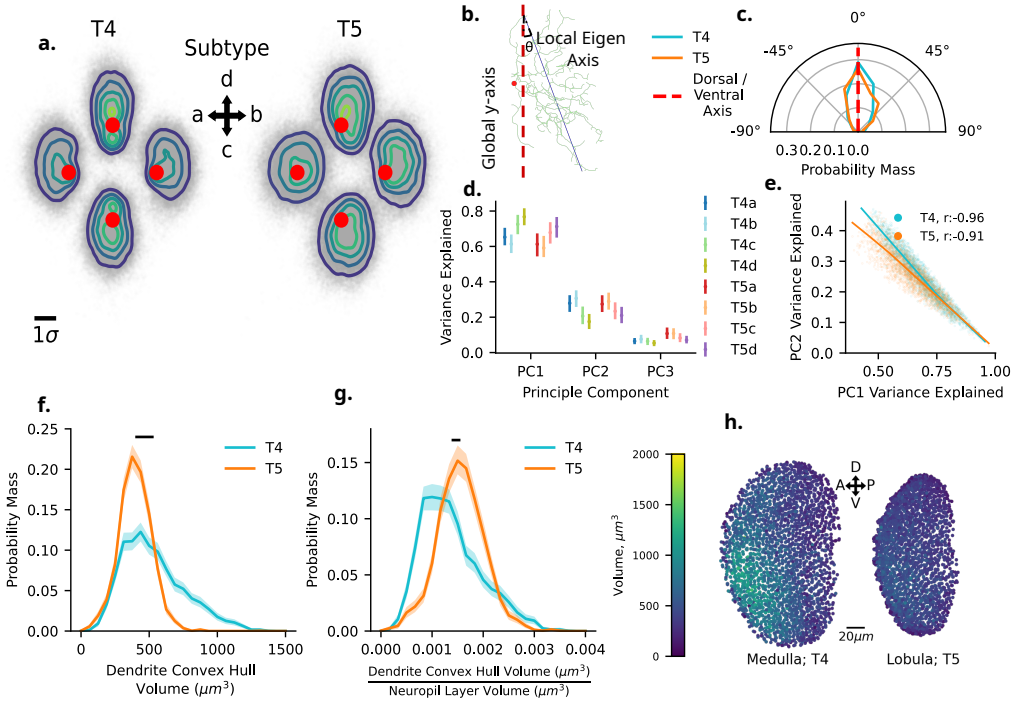

Fig 2. Spatial Embedding and Volume of T4 and T5 Dendrites. a) Scaled and locally aligned subtype specific dendrite populations. Each individual dendrite is aligned to its internal principle axis and scaled within each type specific population (T4 and T5) to one standard deviation of the population dispersion along the first principle axis. Individual dendrites are centred on the root of the dendritic tree (red points). KDE's show point density for each subtype. b) Schematic illustrating angular deviation between a dendrites internal first principle axis (blue line) and the global Dorsal-Ventral (DV) axis (red dashed line). Red point shows the dendrite root. c) Distribution of angles between DV axis and dendrites first principle axis to T4 and T5 dendrite d) Variance explained along each principle component (ranked eigenvalues) for each subtype. e) Correlation of variance explained between first and second principle components for T4 and T5 dendrites. f) Distribution of raw convex hull volumes for T4 and T5 dendrites. Black horizontal lines denotes difference in means. g) Distribution of convex hull volumes scaled by Medulla layer 10 volume (T4) and Lobula layer 1 volume (T5). Black horizontal lines denotes difference in means. h) Spatial distribution of T4 and T5 convex hull volumes within their respective neuropil (T4, Medulla, left; T5, Lobula, right) on the globally aligned DV / AP plane.

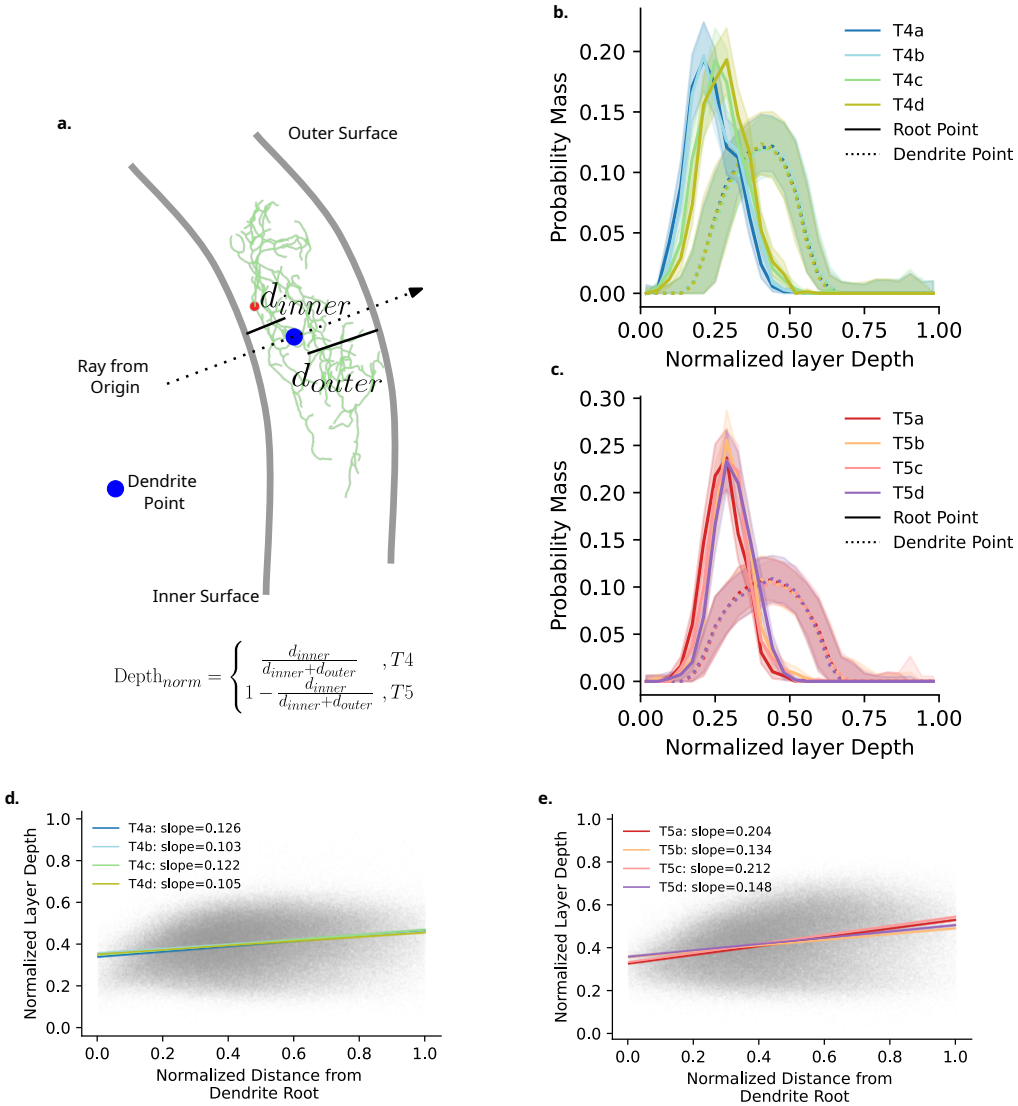

Fig 3. Dendrite Neuropil Layer Specific Depth. a) Schematic illustrating Neuropil specific depth calculation within T4 and T5. Layer surface meshes are generated using all dendrite points, and inner and outer faces estimated using the dot product of a ray from the coordinate origin and the normal of each surface face (See Materials and Methods, Surface Fitting and Volume). For both Medulla Layer 10 and Lobula layer 1, inner and outer surfaces are assigned in the direction of concave curvature. As T5 dendrites innervate from the side of the the outer surface, and T4 from the inner, T5 normalized depths are inverted.b) Distribution of T4 dendrite point depths, grouped horizontal (a,b) and vertical (c,d) subtypes. Solid lines indicate dendrite roots, with a bootstrapped confidence interval around the probability mass function. Dashed lines represent the distribution of non-root points within dendrites, shaded region show asymmetric MAD within the probability mass function across individuals. c) As in b, for T5 dendrites.d) Multiple Regression showing subtype specific slopes within T4 dendrites illustrating the relation ship between normalized node distance from root (path length / longest path in dendrite) and normalized point depth within Medulla layer 10. Root and furthest points within each dendrite ($x = 0$ and $x = 1$) are excluded. e) As d, but for T5 dendrites showing normalized layer depth in Lobula layer 1.

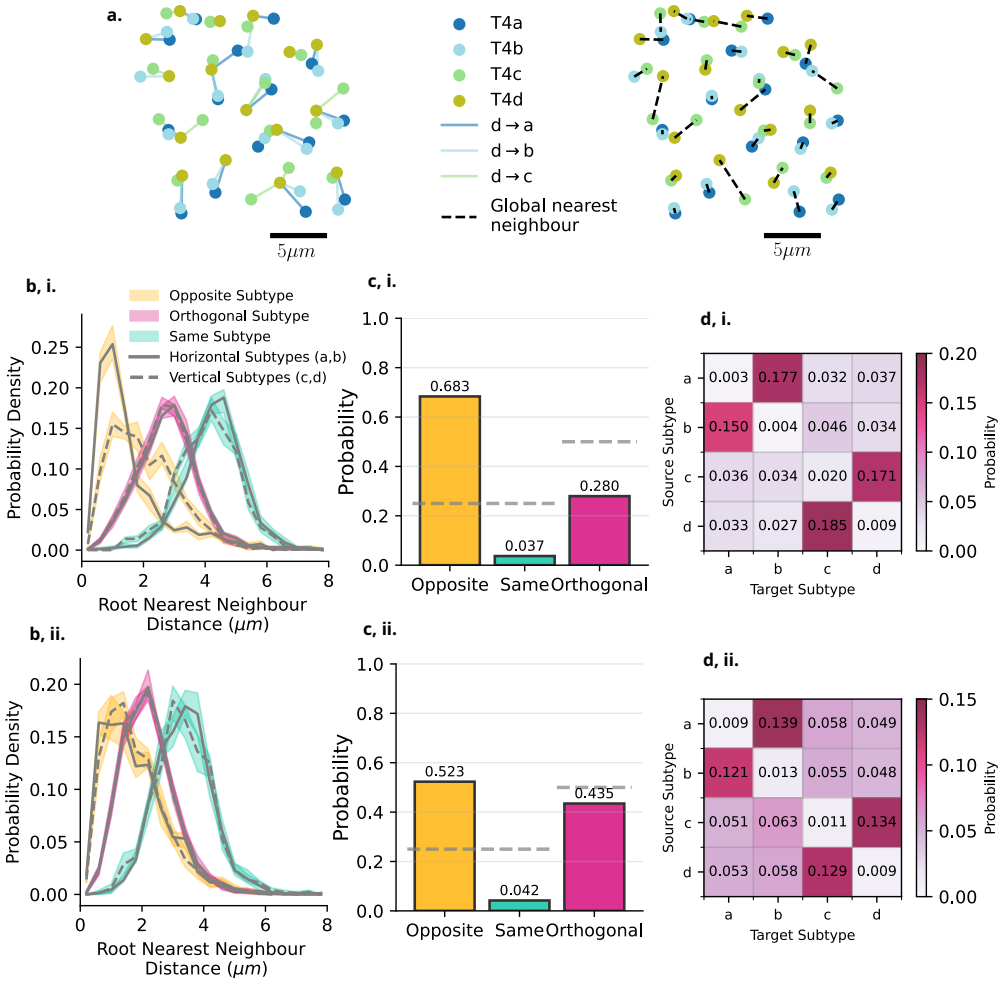

Fig 4. Dendrite root nearest neighbour relationships. a) Illustration of nearest neighbour calculations from a $20\mu m$ section of dendrite root positions within the central medulla. (*left*) shows subtype specific nearest neighbours from T4d dendrites to T4a,b, and c subtypes (T4d→T4d are not shown for simplicity, used in b). (*right*) Global subtype agnostic nearest neighbour calculations determined by using the Hungarian algorithm in order to find the unique set of nearest neighbour pairs which minimises the global distance between pairs of dendrite root points (as used in c,d) b) i: Within subtype nearest neighbour distance distributions for T4 dendrites. Dendrite subtypes are grouped into horizontal (a, b subtypes, solid lines) and vertical (c, d subtypes, dashed lines). "Opposite" distributions denote opposingly oriented subtypes (eg, a→b). "Same" subtypes denote same subtype combinations (eg, a→a). "Orthogonal" denotes orthogonally oriented subtypes (eg, a→c and a→d). ii: As in bi, but for T5 dendrites. c) i: Subtype agnostic probability of global nearest neighbour being of the "Opposite", "Same", or "Orthogonal" group within T4 dendrites. Dashed lines denote approximate chance probability for each group (0.25 for "Opposite" and "Same" groups, 0.5 for "Orthogonal" groups). ii: As in c i, but for T5 dendrites. d) i: Subtype specific nearest neighbour subtype probabilities within T4 dendrites derived from global population nearest neighbour calculations. ii: As in di, but for T5 dendrites.

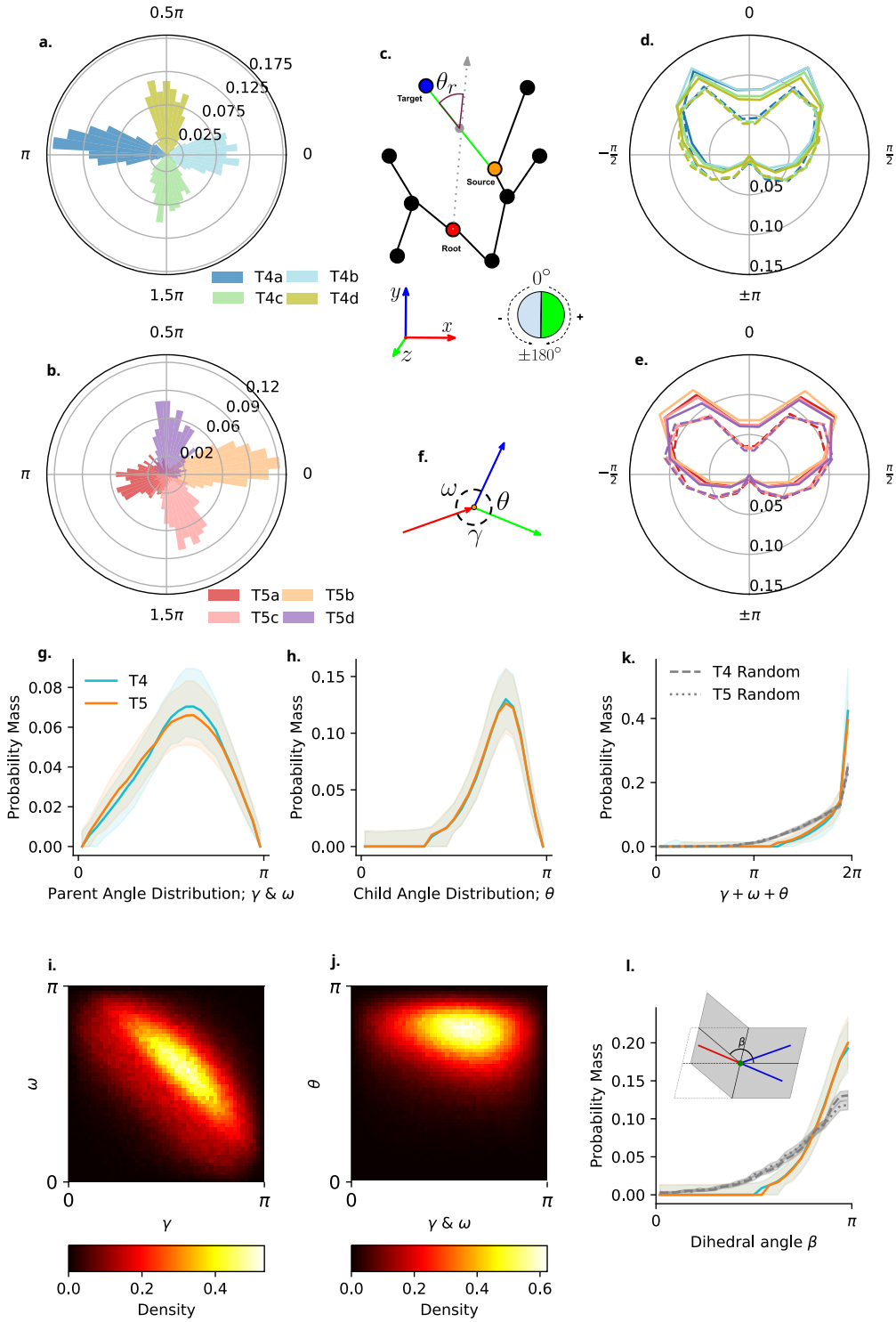
a.
0.5π
0.175
0.125
0.075
0.025
π
0
1.5π
T4a
T4b
T4c
T4d
b.
0.5π
0.12
0.09
0.06
0.02
π
0
1.5π
T5a
T5b
T5c
T5d
c.
Target
Source
Root
θ_r
y
x
z
0°
±180°
d.
0
$-\frac{\pi}{2}$
$\frac{\pi}{2}$
0.05
0.10
0.15
±π
e.
0
$-\frac{\pi}{2}$
$\frac{\pi}{2}$
0.05
0.10
0.15
±π
f.
ω
θ
γ
g.
T4
T5
Probability Mass
0.08
0.06
0.04
0.02
0.00
0
π
Parent Angle Distribution; γ & ω
h.
Probability Mass
0.15
0.10
0.05
0.00
0
π
Child Angle Distribution; θ
k.
T4 Random
T5 Random
Probability Mass
0.4
0.2
0.0
0
π
2π
γ + ω + θ
i.
π
ω
0
0
π
γ
0.0
0.2
0.4
Density
j.
π
θ
0
0
π
γ & ω
0.0
0.2
0.4
0.6
Density
l.
β
Probability Mass
0.20
0.15
0.10
0.05
0.00
0
π
Dihedral angle β

Fig 5. Dendrite orientation and Geometry. a) Distribution of mean section angles for each dendrites relative to the Anterior-Posterior axis, coloured by subtype. b) As in a, for T5 dendrites. c) Schematic illustration of radial angle calculation. Note that $\theta_r = 0$ denotes a section perfectly aligned with the ray cast from the dendrite root (gray dashed arrow). As such, segments where the source node is the dendrite root have $\theta_r = 0$ and are excluded from analysis. Plane normal orientations used for calculation of the sign of θ_r are oriented in the same direction to ensure accurate signs for θ_r. d) Radar plot showing distribution of section radial angles within T4 subtypes. Solid lines show internal dendrite sections, and dashed lines denote external leaf sections. e) As in d, but for T5 dendrites. f) Schematic illustration indicating notation of bifurcation angular components. The red arrow denotes the parent section, and blue and green indicate the two child sections. γ and ω show the angles from the parent section to either of the two child sections. θ denotes the angle between the two child sections. g) Distribution of parent to child angles γ and ω within T4 and T5 dendrites. Shaded region show asymmetric MAD within the probability mass function across individuals. h) Distribution of child angle θ for T4 and T5 dendrites. Line colours are the same as in g. i) Joint probability distribution illustrating inverse relationship between parent to child angles γ and ω. Data for type and subtype are collapsed together. j) Joint probability distribution showing relationship between Parent to child angles γ and ω with child angle θ.k) Distribution of the sum of bifurcation angular components (γ ,ω and θ) for T4 and T5 Dendrites. Gray dashed (T4) and dotted (T5) lines show bifurcation angular component sums for randomly generated bifurcations for comparison (See Materials and Method, Geometry Analysis). l) Distributions of Dihedral angle β, used as a measure of 3D bifurcation flatness for T4 and T5 dendrites. Gray dotted and dashed lines facilitate comparison against randomly generated bifurcations as in k.

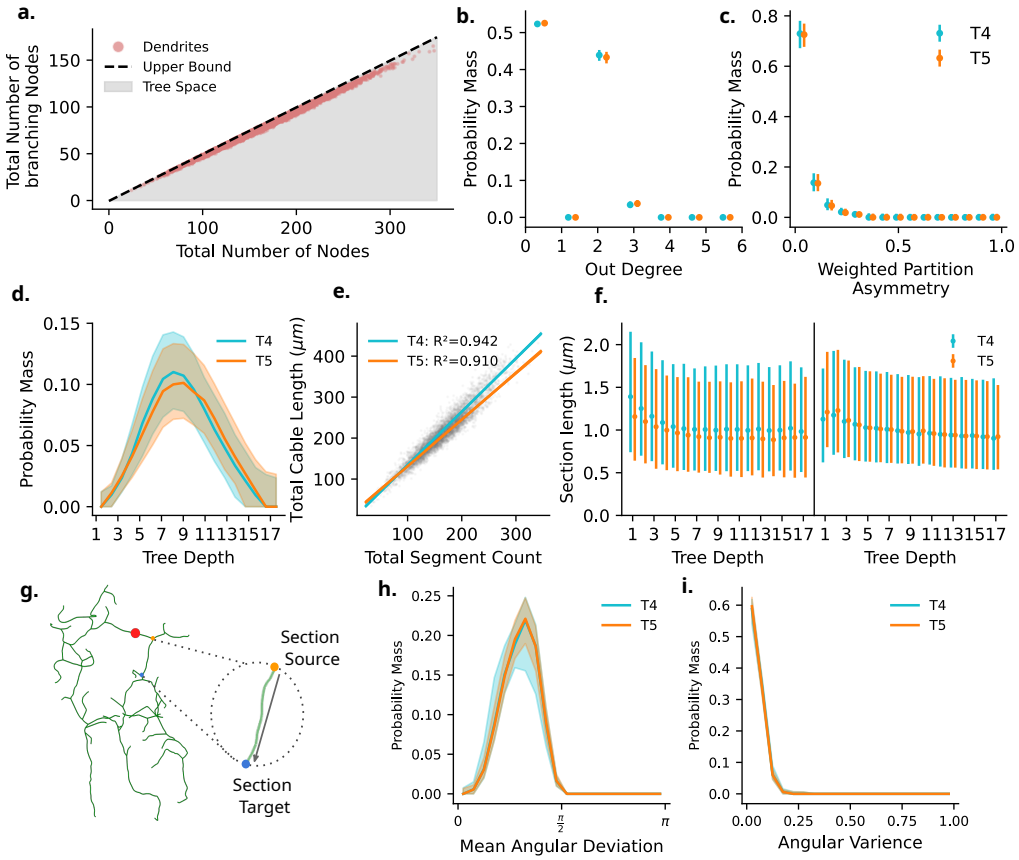

Fig 6. Graphical Structure of Dendrites. a) Scatter plot showing the relationship between total number of nodes and number of branching (internal) nodes within a dendrite tree graph. Gray filled in space denotes the region of possible tree-graphs, where by outside this region a given graph will no longer be a tree-graph. Black dashed line denotes a binary tree. b) Distribution of node out-degree for T4 and T5 dendrites. Nodes with out-degree of 0 are leaf nodes, and and out-degree of 2 show bifurcations. No nodes with an out-degree of 1 exist in the reduced tree-graph representations used (See Materials and Methods, Neurons as Tree Graphs). Error bars show asymmetric MAD of probability mass functions across individual dendrites. c) Distributions of weighted partition asymmetry across T4 and T5 dendrites (See Materials and Methods, Branching Structure and Symmetry Quantification). Values of 0 show symmetric branching and 1 show asymmetry. Error bars show asymmetric MAD of probability mass functions across individual dendrites. d) Relationship between number of dendrite sections and total dendrite cable length in T4 and T5 dendrites. e) Distribution of external (leaf node) counts at increasing dendrite tree-graph depths. Error bars show asymmetric MAD of probability mass functions across individual dendrites. f) Section length with increasing tree-graph depth for both T4 and T5 dendrites in internal (left) and external (right) sections. Error bars show asymmetric MAD of probability mass functions across individual dendrites. g) Schematic illustration showing curvature of individual segments around the euclidean vector between source and target nodes of the section. "Raw" dendrite skeletons are sampled at $10nm$, so a single dendrite tree-graph section is comprised of multiple edges, and the euclidean distance between the source and target of dendrite sections is less than the sum of edge weights. h) Distribution of mean angle between individual edges and their respective euclidean section vector. Error bars show asymmetric MAD of probability mass functions across individual dendrites. i) Angular variance of raw dendrite edges around each dendrite section euclidean vector. Error bars show asymmetric MAD of probability mass functions across individual dendrites.

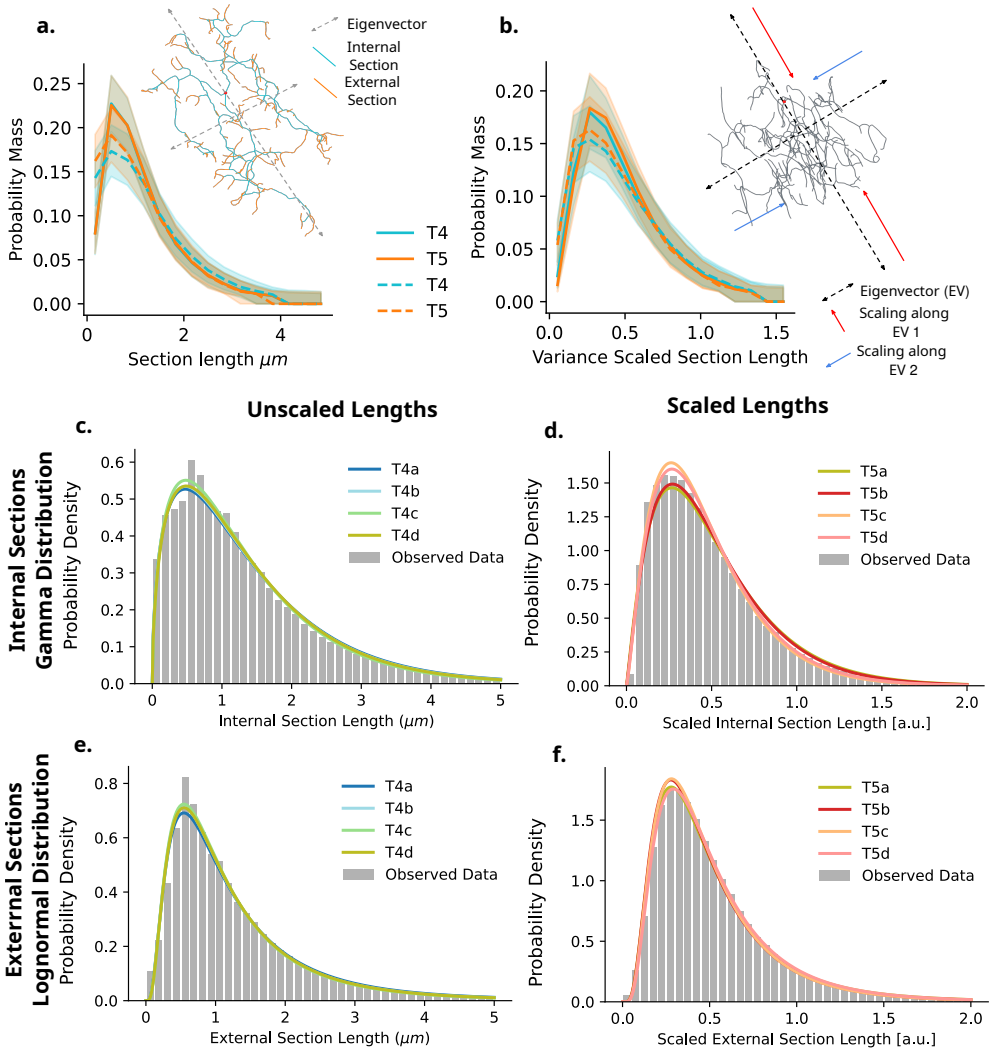

Fig 7. Dendrite Section length Distribution and Explorative Distribution Fitting. a) Distribution of dendrite section lengths for T4 and T5 neurons, with dashed lines showing internal sections and solid lines showing external leaf sections. Schematic (left) shows example neuron with internal (cyan) and external (orange) sections coloured for illustration, along with first two eigenvectors. b) Distribution of section length as in a, but for "variance" scaled dendrites (See Materials and Methods, Alignment and Scaling). Dendrites are individually scaled to have equal variance along each eigenvector in order to account for neuropil specific differences. Insert illustrated scaling. c) Best fitting tested distribution for unscaled internal section lengths (gamma distribution) d) Best fitting tested distribution for scaled internal section lengths (gamma distribution) e) Best fitting tested distribution for unscaled external section lengths (log-normal distribution) f) Best fitting tested distribution for scaled external section lengths (log-normal distribution). Error bars in a,b, show asymmetric MAD of probability mass functions across individual dendrites. Histograms and fits are pooled over type and subtype.

Supporting information

S1 Fig. Supplementary Figure 1: Distribution and Correlations of Size Based Dendrite Metrics. a) Probability mass function of total dendrite cable lengths. b) Spatial distribution of total dendrite cable length. c) Correlation between total dendrite cable length and dendrite convex hull volume. d) Probability mass function of total number of dendrite sections. e) Spatial distribution of total number of dendrite sections. f) Correlation between total number of dendrite sections and convex hull volume.

S2 Fig. Supplementary Figure 2: T4 Log-likelihoods from cross validation for each model distribution for internal sections (left column) and external sections (right column), for each subtype (rows)

S3 Fig. Supplementary Figure 3: T5 Log-likelihoods from cross validation for each model distribution for internal sections (left column) and external sections (right column), for each subtype (rows)

S1 Table. Counts of all available and included neuron morphologies before and after dendrite annotation.

Acknowledgments

We are grateful to all members of the Borst Department for helpful comments and discussion of the manuscript and analysis. We thank the Princeton FlyWire team and members of the Murthy and Seung labs for development and maintenance of FlyWire (supported by BRAIN Initiative grant MH117815 to Murthy and Seung). We also acknowledge members of the Princeton FlyWire team and the FlyWire consortium for neuron proofreading.

Author Contributions

N.Drummond, A.Zhao, and A.Borst conceived the study and wrote the manuscript. N.Drummond and A.Zhao determined the analysis pipeline. N.Drummond implemented software tools.

References

1. Meinertzhagen IA, Takemura Sy, Meinertzhagen IA, Takemura Sy, Lu Z, Huang S, et al. From Form to Function: The Ways to Know a Neuron;23(1–2):68–77. doi:10.1080/01677060802610604.

2. Parekh R, Ascoli GA. Neuronal Morphology Goes Digital: A Research Hub for Cellular and System Neuroscience;77(6):1017–1038. doi:10.1016/j.neuron.2013.03.008.

3. Shomar A, Geyrhofer L, Ziv NE, Brenner N. Cooperative Stochastic Binding and Unbinding Explain Synaptic Size Dynamics and Statistics;13(7):e1005668. doi:10.1371/journal.pcbi.1005668.

4. Ascoli GA. Neuroinformatics Grand Challenges;6(1):1–3. doi:10.1007/s12021-008-9010-5.

5. Costa LdF, Manoel ETM, Faucereau F, Chelly J, family=Pelt pu given=Jaap, Ramakers G. A Shape Analysis Framework for Neuromorphometry;13(3):283–310. doi:10.1088/0954-898X-13-3303.

6. Dorkenwald S, McKellar CE, Macrina T, Kemnitz N, Lee K, Lu R, et al. FlyWire: Online Community for Whole-Brain Connectomics;19(1):119–128. doi:10.1038/s41592-021-01330-0.

7. Dorkenwald S, Matsliah A, Sterling AR, Schlegel P, Yu Sc, McKellar CE, et al. Neuronal Wiring Diagram of an Adult Brain;634(8032):124–138. doi:10.1038/s41586-024-07558-y.

8. Schlegel P, Yin Y, Bates AS, Dorkenwald S, Eichler K, Brooks P, et al. Whole-Brain Annotation and Multi-Connectome Cell Typing of Drosophila;634(8032):139–152. doi:10.1038/s41586-024-07686-5.

9. Matsliah A, Yu Sc, Kruk K, Bland D, Burke AT, Gager J, et al. Neuronal Parts List and Wiring Diagram for a Visual System;634(8032):166–180. doi:10.1038/s41586-024-07981-1.

10. Buhmann J, Sheridan A, Malin-Mayor C, Schlegel P, Gerhard S, Kazimiers T, et al. Automatic Detection of Synaptic Partners in a Whole-Brain Drosophila Electron Microscopy Data Set;18(7):771–774. doi:10.1038/s41592-021-01183-7.

11. Heinrich L, Funke J, Pape C, Nunez-Iglesias J, Saalfeld S. Synaptic Cleft Segmentation in Non-isotropic Volume Electron Microscopy of the Complete Drosophila Brain. In: Frangi AF, Schnabel JA, Davatzikos C, Alberola-López C, Fichtinger G, editors. Medical Image Computing and Computer Assisted Intervention – MICCAI 2018. Springer International Publishing;. p. 317–325.

12. Eckstein N, Bates AS, Champion A, Du M, Yin Y, Schlegel P, et al. Neurotransmitter Classification from Electron Microscopy Images at Synaptic Sites in Drosophila Melanogaster;187(10):2574–2594.e23. doi:10.1016/j.cell.2024.03.016.

13. Nern A, Loesche F, Takemura Sy, Burnett LE, Dreher M, Gruntman E, et al.. Connectome-Driven Neural Inventory of a Complete Visual System;. Available from: `https://www.biorxiv.org/content/10.1101/2024.04.16.589741v2`.

14. Berg S, Beckett IR, Costa M, Schlegel P, Januszewski M, Marin EC, et al.. Sexual Dimorphism in the Complete Connectome of the Drosophila Male Central Nervous System;. Available from: `https://www.biorxiv.org/content/10.1101/2025.10.09.680999v1`.

15. Shiu PK, Sterne GR, Spiller N, Franconville R, Sandoval A, Zhou J, et al. A Drosophila Computational Brain Model Reveals Sensorimotor Processing;634(8032):210–219. doi:10.1038/s41586-024-07763-9.

16. Valdes-Aleman J, Fetter RD, Sales EC, Heckman EL, Venkatasubramanian L, Doe CQ, et al. Comparative Connectomics Reveals How Partner Identity, Location, and Activity Specify Synaptic Connectivity in Drosophila;109(1):105–122.e7. doi:10.1016/j.neuron.2020.10.004.

17. Stürner T, Brooks P, Capdevila LS, Morris BJ, Javier A, Fang S, et al.. Comparative Connectomics of the Descending and Ascending Neurons of the Drosophila Nervous System: Stereotypy and Sexual Dimorphism;. Available from: `https://www.biorxiv.org/content/10.1101/2024.06.04.596633v2`.

18. Haber A, Wanner AA, Friedrich RW, Schneidman E. The Structure and Function of Neural Connectomes Are Shaped by a Small Number of Design Principles;. Available from: https://www.biorxiv.org/content/10.1101/2023.03.15.532611v1.

19. Richter O, Schneidman E. Building a Small Brain with a Simple Stochastic Generative Model;. Available from: https://www.biorxiv.org/content/10.1101/2024.07.01.601562v1.

20. Joesch M, Schnell B, Raghu SV, Reiff DF, Borst A. ON and OFF Pathways in Drosophila Motion Vision;468(7321):300–304. doi:10.1038/nature09545.

21. Borst A, Groschner LN. How Flies See Motion;46:17–37. doi:10.1146/annurev-neuro-080422-111929.

22. Maisak MS, Haag J, Ammer G, Serbe E, Meier M, Leonhardt A, et al. A Directional Tuning Map of Drosophila Elementary Motion Detectors;500(7461):212–216. doi:10.1038/nature12320.

23. Zhao A, Gruntman E, Nern A, Iyer NA, Rogers EM, Koskela S, et al.. Eye Structure Shapes Neuron Function in Drosophila Motion Vision;. Available from: https://www.biorxiv.org/content/10.1101/2022.12.14.520178v1.

24. Henning M, Ramos-Traslosheros G, Gür B, Silies M. Populations of Local Direction–Selective Cells Encode Global Motion Patterns Generated by Self-Motion;8(3):eabi7112. doi:10.1126/sciadv.abi7112.

25. Shinomiya K, Huang G, Lu Z, Parag T, Xu CS, Aniceto R, et al. Comparisons between the ON- and OFF-edge Motion Pathways in the Drosophila Brain;8:e40025. doi:10.7554/eLife.40025.

26. Haag J, Arenz A, Serbe E, Gabbiani F, Borst A. Complementary Mechanisms Create Direction Selectivity in the Fly;5:e17421. doi:10.7554/eLife.17421.

27. Pinto-Teixeira F, Koo C, Rossi AM, Neriec N, Bertet C, Li X, et al. Development of Concurrent Retinotopic Maps in the Fly Motion Detection Circuit;173(2):485–498.e11. doi:10.1016/j.cell.2018.02.053.

28. Hörmann N, Schilling T, Ali AH, Serbe E, Mayer C, Borst A, et al. A Combinatorial Code of Transcription Factors Specifies Subtypes of Visual Motion-Sensing Neurons in Drosophila;147(9):dev186296. doi:10.1242/dev.186296.

29. Takemura Sy, Nern A, Chklovskii DB, Scheffer LK, Rubin GM, Meinertzhagen IA. The Comprehensive Connectome of a Neural Substrate for 'ON' Motion Detection in Drosophila;6:e24394. doi:10.7554/eLife.24394.

30. Spanos A. Revisiting the Large n (Sample Size) Problem: How to Avert Spurious Significance Results;6(4):1323–1338. doi:10.3390/stats6040081.

31. Sullivan GM, Feinn R. Using Effect Size—or Why the P Value Is Not Enough;4(3):279–282. doi:10.4300/JGME-D-12-00156.1.

32. Lakens D. Calculating and Reporting Effect Sizes to Facilitate Cumulative Science: A Practical Primer for t-Tests and ANOVAs;4. doi:10.3389/fpsyg.2013.00863.

33. Cohen J. Statistical Power Analysis for the Behavioral Sciences, Rev. Ed. Statistical Power Analysis for the Behavioral Sciences, Rev. Ed. Lawrence Erlbaum Associates, Inc;.

34. Meier M, Borst A. Extreme Compartmentalization in a Drosophila Amacrine Cell;29(9):1545–1550.e2. doi:10.1016/j.cub.2019.03.070.

35. Schneider-Mizell CM, Gerhard S, Longair M, Kazimiers T, Li F, Zwart MF, et al. Quantitative Neuroanatomy for Connectomics in Drosophila;5:e12059. doi:10.7554/eLife.12059.

36. Bates AS, Schlegel P, Roberts RJV, Drummond N, Tamimi IFM, Turnbull R, et al. Complete Connectomic Reconstruction of Olfactory Projection Neurons in the Fly Brain;30(16):3183–3199.e6. doi:10.1016/j.cub.2020.06.042.

37. Buffry AD, Currea JP, Franke-Gerth FA, Palavalli-Nettimi R, Bodey AJ, Rau C, et al. Evolution of Compound Eye Morphology Underlies Differences in Vision between Closely Related Drosophila Species;22(1):67. doi:10.1186/s12915-024-01864-7.

38. Posnien N, Hopfen C, Hilbrant M, Ramos-Womack M, Murat S, Schönauer A, et al. Evolution of Eye Morphology and Rhodopsin Expression in the Drosophila Melanogaster Species Subgroup;7(5):e37346. doi:10.1371/journal.pone.0037346.

39. Choi BJ, Chen YC, Desplan C. Retinal Calcium Waves Coordinate Uniform Tissue Patterning of the Drosophila Eye;. Available from: https://www.biorxiv.org/content/10.1101/2025.06.02.657513v1.

40. Ouyang X, Sutradhar S, Trottier O, Shree S, Yu Q, Tu Y, et al. Neurons Exploit Stochastic Growth to Rapidly and Economically Build Dense Radially Oriented Dendritic Arbors; p. 2025.02.24.639873. doi:10.1101/2025.02.24.639873.

41. Shree S, Sutradhar S, Trottier O, Tu Y, Liang X, Howard J. Dynamic Instability of Dendrite Tips Generates the Highly Branched Morphologies of Sensory Neurons;8(26):eabn0080. doi:10.1126/sciadv.abn0080.

42. Cuntz H, Forstner F, Borst A, Häusser M. One Rule to Grow Them All: A General Theory of Neuronal Branching and Its Practical Application;6(8):e1000877. doi:10.1371/journal.pcbi.1000877.

43. family=Pelt pu given=Jaap, Uylings HBM. The Flatness of Bifurcations in 3D Dendritic Trees: An Optimal Design;5:54. doi:10.3389/fncom.2011.00054.

44. Uylings HBM, Kuypers K, Diamond MC, Veltman WAM. Effects of Differential Environments on Plasticity of Dendrites of Cortical Pyramidal Neurons in Adult Rats;62(3):658–677. doi:10.1016/0014-4886(78)90276-5.

45. Uylings HBM, Kuypers K, Veltman WAM. Environmental Influences on the Neocortex in Later Life. In: Corner MA, Baker RE, Vandepoll NE, Swaab DF, Uylings HBM, editors. Progress in Brain Research. vol. 48 of Maturation of the Nervous System. Elsevier;. p. 261–274. Available from: https://www.sciencedirect.com/science/article/pii/S0079612308610286.

46. Kim Y, Sinclair R, De Schutter E. Local Planar Dendritic Structure: A Uniquely Biological Phenomenon?;10(1):P4. doi:10.1186/1471-2202-10-S1-P4.

47. family=Berg pu given=Mark. Computational Geometry: Algorithms and Applications. Springer Science & Business Media;.

48. Van Pelt J, Uylings HBM, Verwer RWH, Pentney RJ, Woldenberg MJ. Tree Asymmetry—A Sensitive and Practical Measure for Binary Topological Trees;54(5):759–784. doi:10.1016/S0092-8240(05)80142-9.

49. Costa LdF, Zawadzki K, Miazaki M, Viana MP, Taraskin S. Unveiling the Neuromorphological Space;4:150. doi:10.3389/fncom.2010.00150.

50. Kassraian-Fard P, Pfeiffer M, Bauer R. A Generative Growth Model for Thalamocortical Axonal Branching in Primary Visual Cortex;16(2):e1007315. doi:10.1371/journal.pcbi.1007315.

51. Lin C, Xu F, Zhang Y. Brain-Wide Dendrites in a near-Optimal Performance of Dynamic Range and Information Transmission;13(1):7488. doi:10.1038/s41598-023-34454-8.

52. Van Pelt J, Verwer RWH. Growth Models (Including Terminal and Segmental Branching) for Topological Binary Trees;47(3):323–336. doi:10.1007/BF02459919.

53. Kim J, Kwon N, Chang S, Kim KT, Lee D, Kim S, et al. Altered Branching Patterns of Purkinje Cells in Mouse Model for Cortical Development Disorder;1(1):122. doi:10.1038/srep00122.

54. Kawaguchi Y, Karube F, Kubota Y. Dendritic Branch Typing and Spine Expression Patterns in Cortical Nonpyramidal Cells;16(5):696–711. doi:10.1093/cercor/bhj015.

55. Nowakowski RS, Hayes NL, Egger MD. Competitive Interactions during Dendritic Growth: A Simple Stochastic Growth Algorithm;576(1):152–156. doi:10.1016/0006-8993(92)90622-g.

56. Lindsay RD, Scheibel AB. Quantitative Analysis of the Dendritic Branching Pattern of Small Pyramidal Cells from Adult Rat Somesthetic and Visual Cortex;45(3):424–434. doi:10.1016/0014-4886(74)90149-6.

57. Rößler N, Jungenitz T, Sigler A, Bird A, Mittag M, Rhee JS, et al. Skewed Distribution of Spines Is Independent of Presynaptic Transmitter Release and Synaptic Plasticity, and Emerges Early during Adult Neurogenesis;13(8):230063. doi:10.1098/rsob.230063.

58. Loewenstein Y, Kuras A, Rumpel S. Multiplicative Dynamics Underlie the Emergence of the Log-Normal Distribution of Spine Sizes in the Neocortex In Vivo;31(26):9481–9488. doi:10.1523/JNEUROSCI.6130-10.2011.

59. Frank SA. The Common Patterns of Nature;22(8):1563–1585. doi:10.1111/j.1420-9101.2009.01775.x.

60. Limpert E, Stahel WA, Abbt M. Log-Normal Distributions across the Sciences: Keys and Clues: On the Charms of Statistics, and How Mechanical Models Resembling Gambling Machines Offer a Link to a Handy Way to Characterize Log-Normal Distributions, Which Can Provide Deeper Insight into Variability and Probability—Normal or Log-Normal: That Is the Question;51(5):341–352. doi:10.1641/0006-3568(2001)051[0341:LNDATS]2.0.CO;2.

61. Koch AL. The Logarithm in Biology 1. Mechanisms Generating the Log-Normal Distribution Exactly;12(2):276–290. doi:10.1016/0022-5193(66)90119-6.

62. Daley DJ, Vere-Jones D. An Introduction to the Theory of Point Processes. Vol. I. 2nd ed. Probability and Its Applications (New York). Springer-Verlag;.

63. family=Veen pu given=M P, family=Pelt pu given=J. Terminal and Intermediate Segment Lengths in Neuronal Trees with Finite Length;55(2):277–294. doi:10.1007/BF02460884.

64. family=Elburg pu given=Ronald A J. Stochastic Continuous Time Neurite Branching Models with Tree and Segment Dependent Rates;276(1):159–173. doi:10.1016/j.jtbi.2011.01.039.

65. Chou ZZ, Yu GJ, Berger TW. Generation of Granule Cell Dendritic Morphologies by Estimating the Spatial Heterogeneity of Dendritic Branching;14. doi:10.3389/fncom.2020.00023.

66. Stürner T, Tatarnikova A, Mueller J, Schaffran B, Cuntz H, Zhang Y, et al. Transient Localization of the Arp2/3 Complex Initiates Neuronal Dendrite Branching in Vivo;146(7):dev171397. doi:10.1242/dev.171397.

67. Hu X, Viesselmann C, Nam S, Merriam E, Dent EW. Activity-Dependent Dynamic Microtubule Invasion of Dendritic Spines;28(49):13094–13105. doi:10.1523/JNEUROSCI.3074-08.2008.

68. Dehmelt L, Smart FM, Ozer RS, Halpain S. The Role of Microtubule-Associated Protein 2c in the Reorganization of Microtubules and Lamellipodia during Neurite Initiation;23(29):9479–9490. doi:10.1523/JNEUROSCI.23-29-09479.2003.

69. Statman A, Kaufman M, Minerbi A, Ziv NE, Brenner N. Synaptic Size Dynamics as an Effectively Stochastic Process;10(10):e1003846. doi:10.1371/journal.pcbi.1003846.

70. Zipursky SL, Sanes JR. Chemoaffinity Revisited: Dscams, Protocadherins, and Neural Circuit Assembly;143(3):343–353. doi:10.1016/j.cell.2010.10.009.

71. Jan YN, Jan LY. Branching out: Mechanisms of Dendritic Arborization;11(5):316–328. doi:10.1038/nrn2836.

72. Goodman CS, Shatz CJ. Developmental Mechanisms That Generate Precise Patterns of Neuronal Connectivity;72:77–98. doi:10.1016/S0092-8674(05)80030-3.

73. Zhao A, Nern A, Koskela S, Dreher M, Erginkaya M, Laughland CW, et al. A Comprehensive Neuroanatomical Survey of the Drosophila Lobula Plate Tangential Neurons with Predictions for Their Optic Flow Sensitivity; p. 2023.10.16.562634. doi:10.1101/2023.10.16.562634.

74. Schlegel P, Perlman E. Navis-Org/Fafbseg-Py: Version 3.0.10;. Available from: `https://zenodo.org/records/13309663`.

75. Schlegel P, Gokaslan A, Kazimiers T. Navis-Org/Skeletor: Version 1.3.0;. Available from: `https://zenodo.org/records/10900419`.

76. Zheng Z, Lauritzen JS, Perlman E, Robinson CG, Nichols M, Milkie D, et al. A Complete Electron Microscopy Volume of the Brain of Adult Drosophila Melanogaster;174(3):730–743.e22. doi:10.1016/j.cell.2018.06.019.

77. Virtanen P, Gommers R, Oliphant TE, Haberland M, Reddy T, Cournapeau D, et al. SciPy 1.0: Fundamental Algorithms for Scientific Computing in Python;17(3):261–272. doi:10.1038/s41592-019-0686-2.

78. Musy M, Jacquenot G, Dalmasso G, Lee J, Soltwedel J, Pujol L, et al.. Marcomusy/Vedo: 2024.5.2;. Available from: https://doi.org/10.5281/zenodo.11846434.

79. Jammalamadaka SR, SenGupta A. Topics in Circular Statistics. vol. 5. World Scientific Publishing Co. Pte. Ltd.;. Available from: http://dx.doi.org/10.1142/9789812779267.